The Astrophysical Journal, 700:183–198, 2009 July 20 doi:10.1088/0004-637X/700/1/183

INFRARED SPECTROGRAPH SPECTROSCOPY AND MULTI-WAVELENGTH STUDY OF LUMINOUS STAR-FORMING GALAXIES AT $z \simeq 1.9$

J.-S. Huang[1], S. M. Faber[2], E. Daddi[3], E. S. Laird[4], K. Lai[1], A. Omont[5], Y. Wu[6], J. D. Younger[1,7], K. Bundy[8,22], A. Cattaneo[9], S. C. Chapman[10,11], C. J. Conselice[12], M. Dickinson[13], E. Egami[14], G. G. Fazio[1], M. Im[15], D. Koo[2], E. Le Floc'h[16], C. Papovich[17], D. Rigopoulou[18], I. Smail[19], M. Song[15], P. P. Van de Werf[20], T. M. A. Webb[21], C. N. A. Willmer[14], S. P. Willner[1], and L. Yan[6]

[1] Harvard-Smithsonian Center for Astrophysics, 60 Garden Street, Cambridge, MA 02138, USA
[2] University of California Observatories/Lick Observatory, University of California, Santa Cruz, CA 95064, USA
[3] Laboratoire AIM, CEA/DSM-CNRS-Université Paris Diderot, DAPNIA/Service d'Astrophysique, CEA Saclay, Orme des Merisiers, 91191 Gif-sur-Yvette Cedex, France
[4] Astrophysics Group, Imperial College London, Blackett Laboratory, Prince Consort Road, London SW7 2AZ, UK
[5] Institut d'Astrophysique de Paris-CNRS, 98bis Boulevard Arago, F-75014 Paris, France
[6] IPAC, California Institute of Technology, 1200 E. California, Pasadena, CA 91125, USA
[7] Institute for Advanced Study, School of Natural Sciences, Einstein Drive, Princeton, NJ 08540, USA
[8] Department of Astronomy and Astrophysics, University of Toronto, Toronto, ON M5S 3H8, Canada
[9] Astrophysikalisches Institut Potsdam, an der Sternwarte 16, 14482 Potsdam, Germany
[10] Institute of Astronomy, Cambridge, CB3 0HA, UK
[11] University of Victoria, Victoria, BC V8P 1A1, Canada
[12] University of Nottingham, School of Physics & Astronomy, Nottingham NG7 2RD, UK
[13] NOAO, 950 North Cherry Avenue, Tucson, AZ 85719, USA
[14] Steward Observatory, University of Arizona, 933 North Cherry Avenue, Tucson, AZ 85721, USA
[15] Department of Physics and Astronomy, FPRD, Seoul National University, Seoul 151-747, Korea
[16] IfA, University of Hawaii, Honolulu, HI 96822, USA
[17] George P. and Cynthia W. Mitchell Institute for Fundamental Physics and Astronomy, Department of Physics, Texas A&M University, College Station, TX 77843-4242, USA
[18] Department of Astrophysics, Oxford University, Keble Road, Oxford, OX1 3RH, UK
[19] Institute for Computational Cosmology, Durham University, Durham, UK
[20] Leiden Observatory, Leiden University, P.O. Box 9513, NL-2300 RA Leiden, Netherlands
[21] Department of Physics, McGill University, Montréal, QC, Canada
Received 2008 September 25; accepted 2009 April 29; published 2009 July 1

ABSTRACT

We analyze a sample of galaxies chosen to have $F_{24\,\mu\mathrm{m}} > 0.5$ mJy and satisfy a certain IRAC color criterion. Infrared Spectrograph (IRS) spectra yield redshifts, spectral types, and polycyclic aromatic hydrocarbons (PAH) luminosities, to which we add broadband photometry from optical through IRAC wavelengths, MIPS from 24–160 μm, 1.1 mm, and radio at 1.4 GHz. Stellar population modeling and IRS spectra together demonstrate that the double criteria used to select this sample have efficiently isolated massive star-forming galaxies at $z \sim 1.9$. This is the first starburst (SB)-dominated ultraluminous infrared galaxies (ULIRG) sample at high redshift with total infrared luminosity measured directly from FIR and millimeter photometry, and as such gives us the first accurate view of broadband spectral energy distributions for SB galaxies at extremely high luminosity and at all wavelengths. Similar broadband data are assembled for three other galaxy samples—local SB galaxies, local active galactic nucleus (AGN)/ULIRGs, and a second 24 μm-luminous $z \sim 2$ sample dominated by AGN. $L_{\mathrm{PAH}}/L_{\mathrm{IR}}$ for the new $z \sim 2$ SB sample is the highest ever seen, some three times higher than in local SBs, whereas in AGNs this ratio is depressed below the SB trend, often severely. Several pieces of evidence imply that AGNs exist in this SB-dominated sample, except two of which even host very strong AGN, while they still have very strong PAH emission. The Advanced Camera for Surveys images show that most objects have very extended morphologies in the rest-frame ultraviolet band, thus extended distribution of PAH molecules. Such an extended distribution prevents further destruction PAH molecules by central AGNs. We conclude that objects in this sample are ULIRGs powered mainly by SB; and the total infrared luminosity density contributed by this type of objects is 0.9–2.6 $\times 10^7\ L_\odot\ \mathrm{Mpc}^{-3}$.

Key words: cosmology: observations – galaxies: starburst – infrared: galaxies

Online-only material: color figures

1. INTRODUCTION

Formation of massive galaxies provides a critical test of theories of galaxy formation and evolution. Before modern deep observations, the most massive galaxies known were local elliptical galaxies with no ongoing star formation. The classical model for these objects (e.g., Eggen et al. 1962) was monolithic formation at high redshifts, followed by passive evolution. A more recent galaxy formation theory in the cold dark matter (CDM) paradigm (Blumenthal et al. 1984; White & Frenk 1991; Cole et al. 2000) predicts quite the opposite scenario: a galaxy–galaxy merging-tree model. In this scenario, small galaxies formed early in cosmic time, and massive galaxies were assembled later at much lower redshifts by a series of mergers. Observations of local ultra-luminous infrared galaxies (ULIRGs; $L_{\mathrm{IR}} > 10^{12}\ L_\odot$)[23] detected by *IRAS* are consistent

[22] Reinhardt Fellow.

[23] $L_{\mathrm{IR}} \equiv \int_{8\,\mu\mathrm{m}}^{1000\,\mu\mathrm{m}} L_\nu d\nu$ (Sanders & Mirabel 1996).

with the merger theory. Most local ULIRGs have disturbed morphologies, consistent with being merging systems (Kim et al. 2002). ULIRGs in later stages of merging have $r^{-1/4}$ light profiles (James et al. 1999; Rothberg & Joseph 2004). Genzel et al. (2001) and Tacconi et al. (2002) measured local ULIRG dynamical masses and found an average of 10^{11} $M_{\odot}$. These features are consistent with numerical simulation studies of galaxy mergers, indicating that local ULIRGs are merging systems transforming gas-rich galaxies into L_* elliptical galaxies (Kormendy & Sanders 1992; Mihos & Hernquist 1996; Barnes & Hernquist 1996; Tacconi et al. 2002).

The story is different at $z \gtrsim 2$. Deep near-infrared surveys (Franx et al. 2003; Glazebrook et al. 2004; McCarthy et al. 2004; Daddi et al. 2007a; Labbe et al. 2005) have identified apparently luminous passive galaxies already in place at $z \sim 2$, implying that they formed at even higher redshifts. The existence of galaxies with $M_* > 10^{11}$ $M_{\odot}$ at high redshifts may challenge the merger theory of forming such objects at lower redshifts. However, Cattaneo et al. (2008) used a semianalytic model to show that significant numbers of $M_* > 10^{11}$ $M_{\odot}$ galaxies were in places by $z \sim 2$ but many also formed at lower redshifts, that is, there was a whole "downsizing" trend for massive galaxies to form their stars early, but it is merely statistical not absolute. Possibly consistent with this is the fact that the contribution of LIRGs and ULIRGs to the total IR luminosity density is more than 70% at $z = 1$ (Le Floc'h et al. 2005) compared to a negligible percentage locally (Sanders & Mirabel 1996; Huang et al. 2007b). Moreover, the redshift surveys for submillimeter galaxies (SMGs) by Chapman et al. (2003, 2005) reveal a rapidly evolving ULIRG population at $1.7 < z < 2.8$. Such strong evolution is also seen in ULIRGs selected with *BzK* color and MIPS 24 μm flux at $z \sim 2$ with their number density apparently 3 orders of magnitude higher than the local number density. Thus, local ULIRGs would well be the tail end of earlier intense activity.

The *Spitzer* MIPS 24 μm band has been very effective in probing infrared emission from galaxies at redshifts up to $z \sim 3$ (Huang et al. 2005; Webb et al. 2006; Papovich et al. 2006; Rigopoulou et al. 2006; Daddi et al. 2007a, 2007b, 2007c). Papovich et al. (2006), Webb et al. (2006), Daddi et al. (2007b, 2007c), and Dey et al. (2008) argued that 24 μm emission from galaxies at $2 < z < 3$ is powered by both active galactic nuclei (AGNs) and star formation. Spectroscopic observations of a few 24 μm-luminous SMGs and Lyman break galaxies (LBGs) at $1 < z < 3$ (Lutz et al. 2005; Huang et al. 2007a; Le Floc'h et al. 2007; Valiante et al. 2007; Pope et al. 2008) with the Infrared Spectrograph (IRS) on *Spitzer* support this view, showing both strong continua and emission features of polycyclic aromatic hydrocarbons (PAH) in the rest-frame $6 < \lambda < 10$ μm. Systematic infrared spectroscopic surveys of 24 μm-luminous but optically faint sources (Houck et al. 2005; Yan et al. 2005) reveal a dusty, $z \sim 2$ AGN population not detected in optical surveys. Most of these AGNs are ULIRGs with power-law spectral energy distributions (SEDs) in the mid-infrared and deep silicate absorption at 9.7 μm (Sajina et al. 2007a). Weedman et al. (2006b) observed a sample of X-ray AGN with similar properties though generally less silicate absorption. Optically faint radio sources are a mix of AGN and starbursts (SBs; Weedman et al. 2006a) but are predominantly AGN. In general, optically faint objects have weak infrared spectral emission features, and most objects are likely to be AGN (Weedman et al. 2006c). However, not all 24 μm-luminous objects at $z \sim 2$–3 are AGN dominated. For example, Weedman et al. (2006b) and Farrah et al. (2008) also identified samples with an apparent 1.6 μm stellar peak in the IRAC 4.5 or 5.8 μm bands. Both samples show a very narrow redshift distribution due to a selection of the MIPS 24 μm band toward strong 7.7 μm PAH emission at $z \sim 1.9$. IRS spectroscopy of 24 μm-luminous SMGs (Lutz et al. 2005; Menendez-Delmestre et al. 2007; Valiante et al. 2007; Pope et al. 2008; K. Menendez-Delmestre et al. 2009, in preparation) shows similar spectral features, namely, strong PAH emission in objects with a 1.6 μm stellar emission bump (Weedman et al. 2006b; Farrah et al. 2008), indicating intensive star formation in both types of objects.

This paper presents an IRS spectroscopic and multi-wavelength study of a ULIRG sample at $z \sim 2$. The sample comes from the All-wavelength Extended Groth-strip International Survey (AEGIS; Davis et al. 2007), which consists of deep surveys ranging from X-ray to radio wavelengths. Selection of our sample catches a SB-dominated phase of ULIRG with $L_{\rm IR} > 5 \times 10^{12}$ $L_{\odot}$, which is very rare among local ULIRGs. In this paper, we will study their properties including star formation, stellar masses, AGN fractions, and contribution to the universe's star formation history. Section 2 describes the sample selection. The IRS spectroscopic results are presented in Section 3, and Section 4 contains an analysis of stellar populations, star formation rate (SFR), and AGN fraction. Section 5 summarizes our results. All magnitudes are in the AB magnitude system unless stated otherwise, and notation such as "[3.6]" means the AB magnitude at wavelength 3.6 μm. The adopted cosmology parameters are $H_0 = 70$ km s^{-1} Mpc^{-1}, $\Omega_M = 0.3$, and $\Omega_\Lambda = 0.7$.

2. SAMPLE SELECTION

We wish to study the multi-wavelength properties of star-forming galaxies at $z \sim 2$. There are many ways of using optical and NIR colors to select such a sample. The samples with the best spectroscopic confirmation are the *UgR* color-selected BM/BX sources (Steidel et al. 2004), which have estimated typical stellar masses of about 10^9–10^{10} $M_{\odot}$ (Shapley et al. 2005; Reddy et al. 2006, 2008). The average 24 μm flux density for these sources is 42 ± 6 μJy (Reddy et al. 2006), which suggests modest rest-frame mid-IR luminosities, consistent with LIRGs ($L_{\rm IR} < 10^{12}$ $L_{\odot}$). A different sample, based on near-infrared color selection, is the distant red galaxies (DRG; $(J-K)_{\rm vega} > 2.3$) (Franx et al. 2003; Labbe et al. 2005). These galaxies are redder and dustier than the ultraviolet (UV)-selected BM/BX sources and are believed to be more massive than 10^{11} $M_{\odot}$ (Labbe et al. 2005; Papovich et al. 2006). Dusty DRGs have estimated total infrared luminosity in the range $10^{11} < L_{\rm IR} < 10^{12}$ $L_{\odot}$ (Webb et al. 2006; Papovich et al. 2006). A third sample (Daddi et al. 2007a) uses *BzK* colors to select galaxies at $z \sim 2$; massive *BzK* galaxies are mid-IR luminous. Reddy et al. (2005) compared BM/BX, DRGs, and *BzK* galaxies and found that *BzK* galaxies include most DRGs and BM/BX galaxies. This comparison is nicely shown in Figure 9 of Reddy et al. (2005).

An independent way to select galaxies at $z > 1.5$ is to use IRAC colors. In $1.5 < z < 3.0$, the four IRAC bands probe the rest-frame NIR bands where galaxy SEDs have similar shape, thus the IRAC colors are very robust in determining redshift in this range (Huang et al. 2004; Papovich et al. 2008). The 1.6 μm stellar emission bump can be used to separate galaxies at $z = 1.5$. At $z < 1.5$, the IRAC 3.6 and 4.5 μm bands sample galaxy SED from the Jeans tail of cold stars, thus the

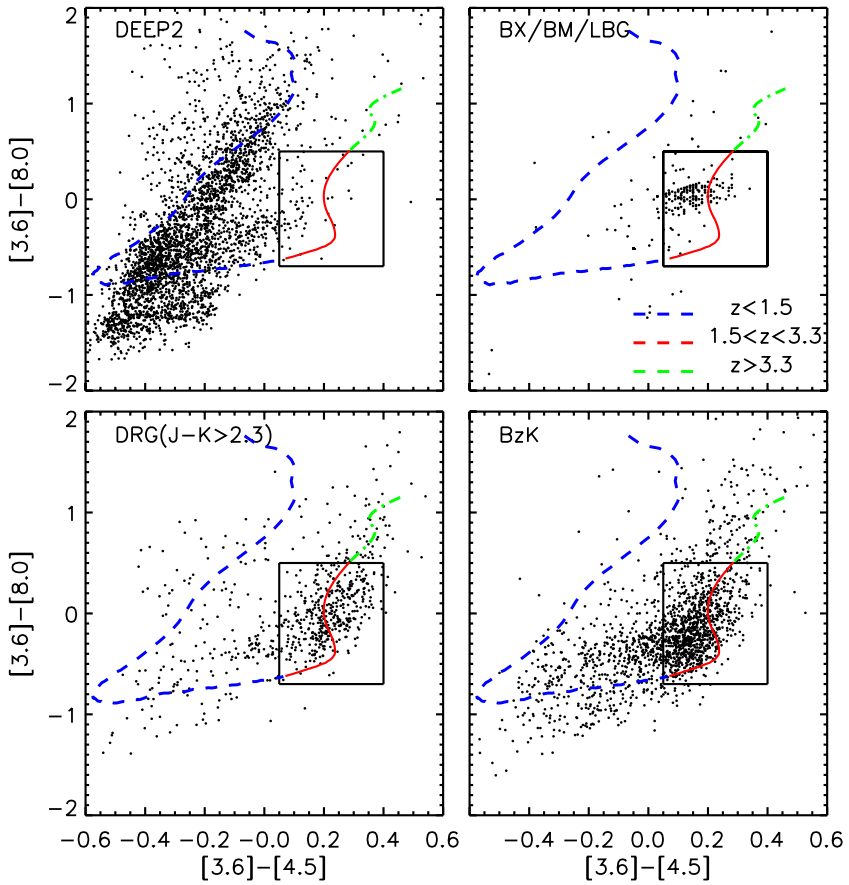

Figure 1. IRAC color–color diagram for several samples. The upper left panel is for the entire AEGIS spectroscopic redshift sample with $0 < z < 1.5$; the upper right panel is for the combined BM/BX and LBG samples with confirmed spectroscopic redshifts (Steidel et al. 2004; Reddy et al. 2008); the lower left panel is for the DRGs (Franx et al. 2003); and the lower right panel is for *BzK* galaxies (Daddi et al. 2007a). The boxes in each panel denote the IRAC color selection for the present sample. The track for the M82 template is also plotted in each panel. The rest-frame UV-selected BM/BX and LBG galaxies have generally faint IRAC flux densities and thus larger photometric uncertainties (Huang et al. 2005; Rigopoulou et al. 2006), increasing the apparent scatter in the upper right panel.

(A color version of this figure is available in the online journal.)

$[3.6] - [4.5] < 0$. At $z \gtrsim 1.5$, the 1.6 μm stellar emission bump begins to move into the IRAC 4.5 μm band, making the $[3.6] - [4.5] > 0$. The color criterion is set based on the M82 SED model (Huang et al. 2004)

$$0.05 < [3.6] - [4.5] < 0.4, \text{ and} \quad (1)$$

$$-0.7 < [3.6] - [8.0] < 0.5. \quad (2)$$

Both color ranges are corresponding to redshift range of $1.5 \lesssim z \lesssim 3.3$. The red color cut in both equations rejects power-law AGNs and star-forming galaxies at $z > 3.3$ whose 7.7 μm PAH shifts out of the IRS wavelength range. The selection is based on the rest-frame NIR colors, and is thus less affected by dust extinction, stellar ages, and metallicities. Figure 1 compares IRAC two-color plots for the DEEP2 galaxies with $z < 1.5$ to LBGs, DRGs, and *BzK* galaxies. The color criteria of Equations (1) and (2) include most galaxies in the $1.5 \lesssim z \lesssim 3.0$ range. Although 8 μm detection is required for this selection method, selecting at this wavelength has some additional advantages. Chosen at roughly 2–3 μm rest frame, the sample selection is immune to dust reddening and is roughly equivalent to a stellar-mass-selected sample. It is thus ideal for studying luminous, potentially massive galaxies (Huang et al. 2004, 2005; Conselice et al. 2007).

The specific IRS targets for this program were selected from a 24 μm sample (Papovich et al. 2004) in the Extended Groth Strip (EGS) region. These sources show a clump at the predicted colors for $1.5 < z < 3$ in Figure 2, but redshifts were not known in advance. Individual targets were selected to have IRAC colors satisfying Equations (1) and (2) and also $F_{24\,\mu\mathrm{m}} > 0.5$ mJy. In addition, each candidate was visually examined in the deep Subaru *R*-band image (M. Ashby et al. 2009, in preparation) to avoid confused or blended targets. With these criteria, 12 targets were selected in the $2^\circ \times 10'$ EGS region for IRS observation. Table 1 lists the sample galaxies. In this redshift range, most sources will be either ULIRGs with total infrared luminosity $L_{\mathrm{IR}} > 10^{12}\ L_\odot$[24] or AGNs with high mid-IR luminosities. For convenience, the galaxy nicknames used in the *Spitzer* database are used in this paper, but these do not follow proper naming conventions and should not be used as sole object identifiers. Proper names are also given in Table 1.

Most of the previous IRS surveys of IR luminous sources at $z \sim 2$ have used rather different selection criteria. Table 2 summarizes the sample criteria for various other IRS surveys. Houck et al. (2005) and Yan et al. (2005) used extreme optical-to-24 μm color to select dusty objects. Objects in these samples have much redder $[3.6] - [8.0]$ IRAC colors than the majority of 24 μm sources (Figure 2) and are mostly AGNs as shown by their

[24] The total infrared luminosities (L_{IR}) for our sample are calculated with MIPS 24, 70, 160 μm, and 1.1 mm flux densities and Chary–Elbaz (Chary & Elbaz 2001; Daddi et al. 2007b, 2007c) SED models. Details are given in Section 4.2.

Table 1
IRS Observation Parameters

Nickname[a]	EGSIRAC[b]	R.A.	Decl.	$F(24\ \mu m)$	Cycles	Exp Time
		J2000		(mJy)		(s)
EGS1	J142301.49+533222.4	14:23:01.50	+53:32:22.6	0.55	10	7314
EGS4	J142148.49+531534.5	14:21:48.49	+53:15:34.5	0.56	10	7314
EGS10	J141928.10+524342.1	14:19:28.09	+52:43:42.2	0.62	8	5851
EGS11	J141920.44+525037.7	14:19:17.44	+52:49:21.5	0.59	8	5851
EGS12	J141917.45+524921.5	14:19:20.45	+52:50:37.9	0.74	5	3657
EGS14	J141900.24+524948.3	14:19:00.27	+52:49:48.1	1.05	3	2194
EGS23	J141822.47+523937.7	14:18:22.48	+52:39:37.9	0.67	7	5120
EGS24	J141834.58+524505.9	14:18:34.55	+52:45:06.3	0.66	7	5120
EGS24a[c]	J141836.77+524603.9	14:18:36.77	+52:46:03.9	0.66	7	5120
EGS26	J141746.22+523322.2	14:17:46.22	+52:33:22.4	0.49	11	8045
EGS_b2	J142219.81+531950.3	14:22:19.80	+53:19:50.4	0.62	8	5851
EGS_b6	J142102.68+530224.5	14:21:02.67	+53:02:24.8	0.72	6	4388

Notes. R.A. and decl. are the commanded telescope pointing coordinates. Telescope pointing was based on high accuracy peakup on nearby 2MASS catalog objects with the blue peak-up array. Ramp duration was 120 s for all objects.
[a] Nicknames are the target names in the *Spitzer* archive and are used for convenience in this paper, but they are not official names and should not be used as standalone source identifications.
[b] Source name from Barmby et al. (2008).
[c] Serendipitous source found in the slit while observing EGS24.

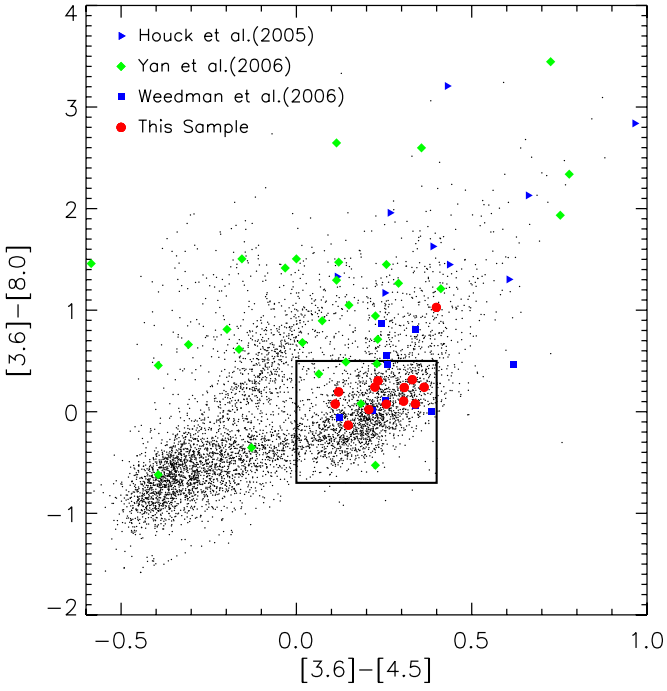

Figure 2. IRAC color–color diagram for EGS galaxies with $F(24\ \mu m) > 80\ \mu$Jy. Small dots show all such galaxies; large red dots show galaxies in the current IRS spectroscopic sample, which also requires $F(24\ \mu m) > 500\ \mu$Jy. The black box shows the IRAC color criteria, which should select objects at $z > 1.5$. The one red dot outside the selection box is the serendipitous source EGS24a. Objects from other IRS spectroscopic samples (Table 1) at $z \sim 2$ are plotted for comparison: the blue triangles and green diamonds denote "optically invisible" sources (Houck et al. 2005; Yan et al. 2005). The blue squares denote the luminous starbursts of Weedman et al. (2006b).

(A color version of this figure is available in the online journal.)

strong power-law continua, but weak or absent PAH emission features (Houck et al. 2005; Yan et al. 2005). Weedman et al. (2006b) selected AGN using similar criteria. They also selected a separate SB-dominated sample at $z \sim 2$ based on the stellar 1.6 μm emission bump. The exact criterion required the peak flux density to be at either 4.5 μm or 5.8 μm, thus rejects low-redshift galaxies and AGN with strong power-law SEDs. The resulting sample is very similar to ours though overall a bit redder (Figure 2). All objects in the Weedman et al. SB sample show strong PAH emission features.

3. IRS SPECTROSCOPY

3.1. Observations and Data Reduction

IRS observations of this sample are part of the GTO program for the *Spitzer*/IRAC instrument team (program ID: 30327). Objects were observed only with the IRS Long-Slit Low-Resolution first-order (LL1) mode, giving wavelength coverage $20 < \lambda < 38\ \mu$m with spectral resolution $60 \lesssim \lambda/\Delta\lambda \lesssim 120$. The wavelength coverage corresponds to $6 \lesssim \lambda \lesssim 13\ \mu$m in the rest frame for galaxies at $z \approx 2$. This wavelength range includes strong PAH emission features at 7.7, 8.6, and 11.3 μm and silicate absorption from 8 to 13 μm (peaking near 9.7 μm). Detecting these features permits redshift measurement and study of dust properties. Total exposure time for each target was based on its 24 μm flux density. Mapping mode (Teplitz et al. 2007) was used to place each object at six positions spaced 24″ apart along the 168″ IRS slit. This not only gives more uniform spectra for the target objects, rejecting cosmic rays and bad pixels, but also increases sky coverage for possible serendipitous objects around each target. Table 1 gives the target list and other parameters for the observations. All data were processed with the Spitzer Science Center pipeline, version 13.0. Extraction of source spectra was done with both the SMART analysis package (Higdon et al. 2004) and our customized software. Lack of IRS coverage at $\lambda \lesssim 20\ \mu$m for this sample is compensated with deep *AKARI* 15 μm imaging (M. Im et al. 2009, in preparation). All objects except two outside the *AKARI* area are detected at 15 μm, providing measurement of the continua at rest-frame $\sim$6 μm for galaxies at $z \approx 2$.

Figure 3 presents the IRS spectra. PAH emission features at 7.7 and 11.3 μm and silicate absorption peaking at 9.7 μm are detected from 10 sources, indicating a narrow redshift range of $1.6 < z < 2.1$. The PAH emission features at 7.7 and 11.3 μm show pronounced variations in their profiles and peak wavelengths. Both 7.7 and 11.3 μm PAH features have at least two components (Peeters et al. 2002). For example, the 7.7 μm PAH feature has a blue component at 7.6 μm and

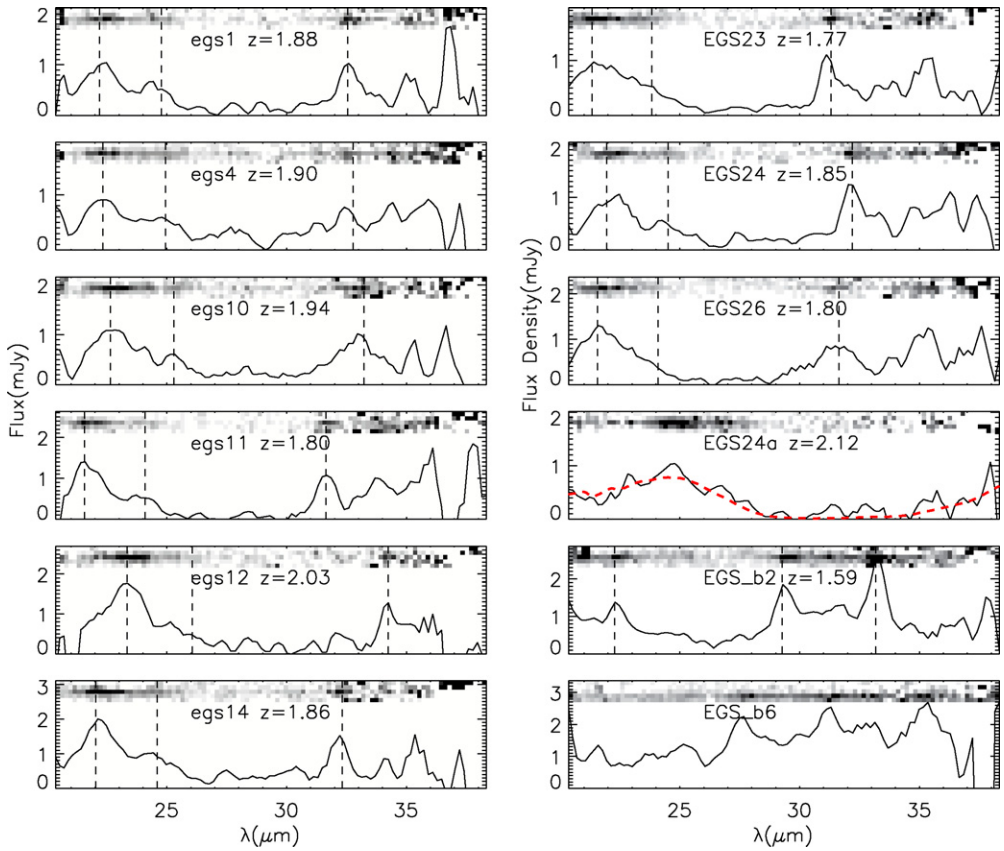

Figure 3. Observed IRS spectra. The vertical scale is linear but different for each panel. The grayscale images are the two-dimensional IRS spectral images after wavelength and position calibration. Each image shows 5 pixels or 25.″5 along the slit. The dashed lines indicate the central wavelengths of the PAH emission features, rest-frame 7.7, 8.6, and 11.3 μm left to right. EGS24a, the serendipitous object in the slit of EGS24, shows a power-law SED with strong silicate absorption. Cross-correlation of the template (red dashed line) of the local ULIRG IRAS F08572+3915 to the spectrum of EGS24a gives $z = 2.12$. For EGS_b2 at $z = 1.59$, the 7.7 μm feature is off scale to the left, and the peak observed at 33.5 μm is the [Ne II] emission line at rest wavelength 12.81 μm. EGS_b6 is a confused case with combining spectra of two galaxies at $z = 1.02$ and $z = 2.0$.

Table 2
IRS Sample Selection Criteria

Sample	24 μm Flux Density (mJy)	Color Criteria
Houck et al. (2005)	>0.75	$\nu F_\nu(24\ \mu\text{m})/\nu F_\nu(I) > 60$
Yan et al. (2005)	>0.9	$\nu F_\nu(24\ \mu\text{m})/\nu F_\nu(I) > 10$ and
		$\nu F_\nu(24\ \mu\text{m})/\nu F_\nu(8\ \mu\text{m}) > 3.16$
Weedman et al. (2006b) (AGN)	>1.0	$F(\text{X-ray})^a \gtrsim 10^{-15}$ erg cm^{-2} s^{-1}
Weedman et al. (2006b) (SB)	>1.0	IRAC flux density peak at either 4.5 or 5.8 μm
This paper	>0.5	$0 < [3.6] - [4.5] < 0.4$ and
		$-0.7 < [3.6] - [8.0] < 0.5$

Note. [a] *Chandra* 0.3–8 keV flux density.

a red component at wavelength longward of 7.7 μm. Thus, different types of PAH spectral templates potentially yield different redshift measurements. To check this, we use two local MIR spectral templates with different PAH profiles, an average local SB spectrum, and an average local ULIRG spectrum to determine redshifts. Both templates yield very similar redshifts (Table 3). The SB template fits all objects better with a typical 2% redshift uncertainty. EGS_b2 is identified at $z = 1.59$ with PAH emission features at 8.6 and 11.3 μm and the [Ne II] emission line at 12.81 μm. Redshift $z = 2.03$ for EGS12 is confirmed by detecting Hα at 1.992 μm (Figure 4) in a NIR spectrum taken with the MOIRC spectrograph on the Subaru telescope (E. Egami et al. 2009, in preparation). The spectrum of EGS_b6, however, shows two emission lines at 27.7 and 31.1 μm that we are not able to identify consistently with any redshift. EGS_b6 is resolved to two objects 0.″7 apart in the *Hubble Space Telescope* (*HST*) Advanced Camera for Surveys (ACS) image (Davis et al. 2007), and an optical spectrum of this system shows two galaxies at $z = 1.02$ and $z = 2.001$. We therefore omit EGS_b6 from the sample for further analysis. The 24 μm images show several serendipitous objects in slits of all 12 targets, most of which are too faint to permit redshift identification. Only one source, EGS24a, have $F_{24\ \mu\text{m}} \sim 1$ mJy. This object, found in the slit of EGS24, shows the silicate absorption feature at $z = 2.12$ (Figure 3).

The redshift distribution of the sample (Figure 5) is very similar to that of the SB-dominated ULIRGs studied by Weedman et al. (2006b), even though our limiting flux density at 24 μm is a factor of two fainter than theirs. Recently, Farrah et al. (2007) use the same criteria to select a larger sample in the Lockman Hole region for the IRS observation and yield a very similar redshift distribution. The narrow distribution for SB-dominated

Table 3
PAH Properties for the Sample

Object	Redshift[a]	Redshift[b]	Log $L(7.7)$ ($L_\odot$)	EW(7.7) (μm)	Log $L(11.3)$ ($L_\odot$)	EW(11.3) (μm)
EGS1	1.95 ± 0.03	1.90 ± 0.02	11.23 ± 0.03	2.38 ± 0.22	10.18 ± 0.15	1.68 ± 0.26
EGS4	1.94 ± 0.03	1.88 ± 0.02	10.89 ± 0.06	0.57 ∓ 0.07	9.82 ± 0.37	0.17 ± 0.07
EGS10	1.94 ± 0.02	1.94 ± 0.01	11.33 ± 0.02	2.39 ± 0.12	10.04 ± 0.31	0.26 ± 0.10
EGS11	1.80 ± 0.02	1.80 ± 0.01	11.02 ± 0.05	0.79 ± 0.10	10.25 ± 0.12	1.19 ± 0.16
EGS12	2.01 ± 0.03	2.02 ± 0.03	11.37 ± 0.02	1.46 ± 0.08	10.61 ± 0.11	1.28 ± 0.55
EGS14	1.87 ± 0.06	1.86 ± 0.03	11.33 ± 0.04	1.13 ± 0.09	10.63 ± 0.10	2.98 ± 0.35
EGS21	3.01 ± 0.03	3.00 ± 0.03	11.73 ± 0.06	1.59 ± 0.10	...	...
EGS23	1.77 ± 0.02	1.77 ± 0.01	11.15 ± 0.04	1.45 ± 0.12	10.54 ± 0.05	1.08 ± 0.08
EGS24	1.85 ± 0.03	1.85 ± 0.01	11.25 ± 0.03	2.24 ± 0.18	10.56 ± 0.07	0.36 ± 0.08
EGS26	1.77 ± 0.03	1.78 ± 0.02	11.16 ± 0.03	2.61 ± 0.20	10.42 ± 0.06	1.12 ± 0.18
EGS_b2	1.59 ± 0.01	1.60 ± 0.01	...	...	10.45 ± 0.04	0.30 ± 0.04

Notes. ... indicates the PAH feature lies outside the observed spectral coverage. EGS24a shows silicate absorption and no PAH emission (Figure 3).
[a] Redshifts obtained with a ULIRG template.
[b] Redshifts obtained with a starburst template.

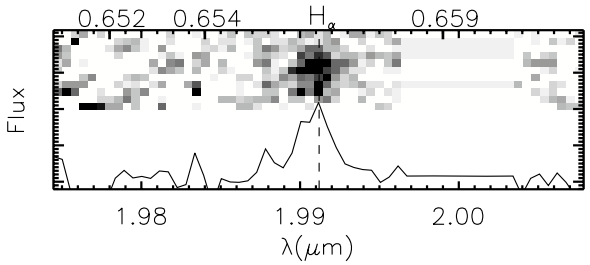

Figure 4. Near-infrared spectrum of EGS12 taken with the MOIRC spectrograph on Subaru. There is nothing detected except one emission line at 1.992 μm. We identify this line as Hα at $z = 2.033$, and corresponding rest-frame wavelengths are marked above the plot. The redshift is consistent with $z = 2.03$ derived from the PAH features in the IRS spectrum (Figure 3).

ULIRGs is due to the selection of strong 7.7 μm PAH emission by the MIPS 24 μm band at $z \sim 1.9$. The peak of the redshift distributions for Weedman et al. (2006b), Farrah et al. (2007), and our sample is at this redshift, confirming the selection effect. On the other hand, luminous 24 μm sources with power-law SED have a much wider redshift range up to $z \sim 3$ (Houck et al. 2005; Yan et al. 2005; Weedman et al. 2006b), but they will not pass our IRAC color criteria or the "bump" SED criterion in Weedman et al. (2006b) and Farrah et al. (2007).

3.2. PAH Emission Features in ULIRGs

The PAH features visible in the individual spectra of the sample galaxies are even more prominent in the average spectrum for the sample, as showed in Figure 6, which also stacks local SB (Brandl et al. 2006) and ULIRG samples for comparison. The local ULIRG sample is divided into Seyfert, LINER, and H II subsamples according to their optical spectral classification (Veilleux et al. 1999). PAH emission features are found have different feature profiles. Peeters et al. (2002) classified profiles of each PAH emission feature, according to the peak wavelength, into three main classes: Class A, B, and C. PAH emission features are known to have more than one component in each feature. For example, the 7.7 μm PAH emission feature has two major components at 7.6 and 7.8 μm: Class A is defined as 7.6 μm-dominated PAH; Class B is the 7.8 μm-component-dominated PAH; and Class C is red-component-dominated with peak shifting beyond 7.8 μm. The 7.7 μm PAH in the local SB spectrum appears to be more consistent with Class A with

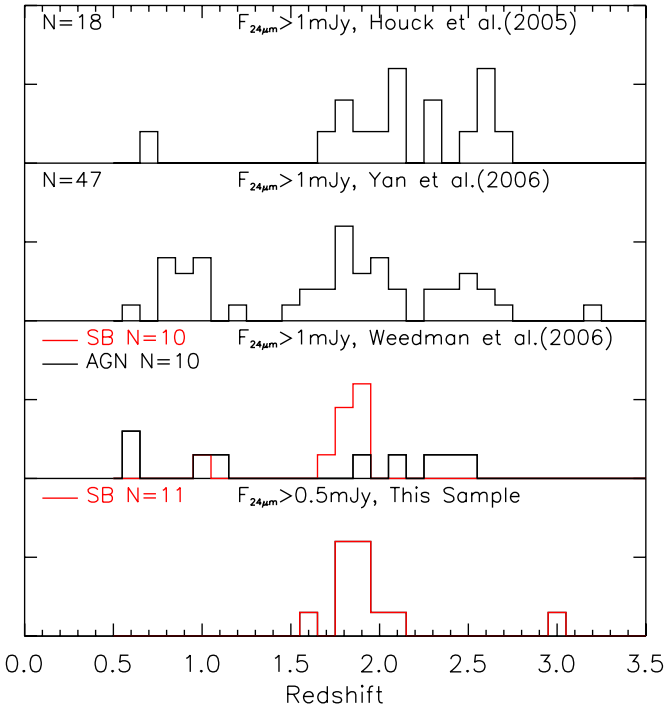

Figure 5. Redshift distributions for spectroscopic samples in Table 1. In the third panel, the red line shows the distribution for the starburst (SB) sample and the black line for the AGN sample.
(A color version of this figure is available in the online journal.)

the peak at wavelength shorter than 7.7 μm. All local ULIRG spectra have a typical Class B PAH profile, with a red wing extending beyond 8 μm. In Section 3.1, we already found that the SB template fits each IRS spectrum of our sample better than the ULIRG template. It is not surprising then that the average 7.7 μm PAH profile of our sample is more similar to the average SB spectrum, thus consistent with the Class A. Another significant difference is that our ULIRG sample has an average $L_{11.3\,\mu m}/L_{7.7\,\mu m}$[25] ratio about twice as high as local ULIRGs but similar to local SBs (Brandl et al. 2006). We also plot the average spectra of Yan et al. (2005) in Figure 6 for

[25] $L_{11.3\,\mu m}$ and $L_{7.7\,\mu m}$ are the 7.7 and 11.3 μm PAH emission luminosities defined as $L_{\rm PAH} = 4\pi d_L^2 \int F_{\rm PAH}(\nu) d\nu$.

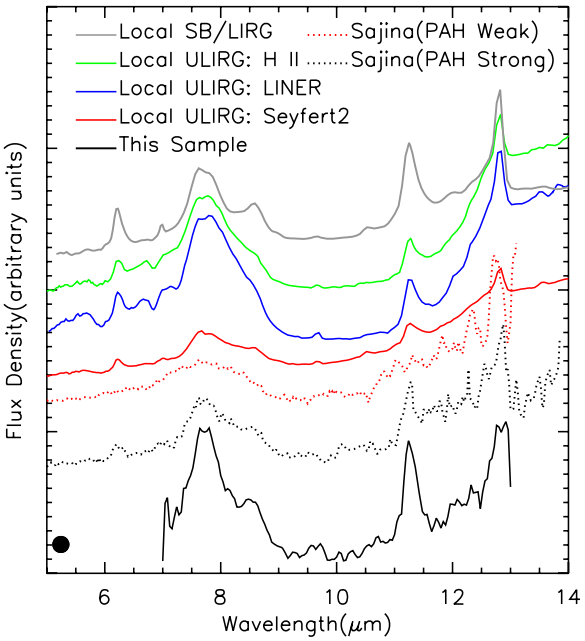

Figure 6. Stacked spectrum for ULIRGs in the present sample (black line). The short wavelength limit for the stacked spectrum is 7 μm. The large dot at rest wavelength 5.3 μm represents the stacked *AKARI* 15 μm flux density. The vertical scale is linear flux density per unit frequency in arbitrary units. Other lines show stacked spectra of comparison samples: local starburst (SB) galaxies (gray line; Brandl et al. 2006), local Seyfert-type ULIRGs (red line), local LINER-type ULIRGs (blue line), and local H II/SB ULIRGs (green line). The local ULIRG samples are from the *IRAS* 1 Jy sample (Kim & Sanders 1998) with IRS observations in the IRS GTO program (PID 105; Farrah et al. 2007; Armus et al. 2007). Types were assigned according to optical spectroscopy (Veilleux et al. 1995, 1999). The average SED of the present sample is very similar to those of local LINER- and H II-type ULIRGs, while average SEDs for objects in Sajina et al. (2007a) are close to the local Seyfert-type ULIRGs with much higher continuum emission.

(A color version of this figure is available in the online journal.)

comparison. The average spectrum for strong PAH objects in Yan et al. (2005) is more similar to the local Seyfert-type ULIRG, implying a dominant AGN contribution in the spectra of their sample. We conclude from IRS stacking that the 7.7 μm PAH profiles and $L_{11.3\ \mu\mathrm{m}}/L_{7.7\ \mu\mathrm{m}}$ ratios for the present sample are more consistent with those of local SB galaxies rather than local ULIRGs.

PAH emission features are a tracer of star formation, one of the energy sources powering ULIRGs (Genzel et al. 1998; Rigopoulou et al. 1999; Sajina et al. 2007a). In order to subtract the local continuum, we adopted the method used by Sajina et al. (2007a), fitting the $5 < \lambda < 15$ μm spectrum into three components: the PAH emission features, a power-law continuum, and the silicate absorption. An iterative fit determined the continuum for each object. The initial input PAH template was from the NGC 7714 IRS spectrum after subtracting its power-law continuum. The silicate absorption profile was from Chiar & Tielens (2006) with central optical depth $\tau_{9.7}$ a free parameter. The 7.7 and 11.3 μm PAH line luminosities and equivalent widths for the local SB sample (Brandl et al. 2006), the local ULIRG sample (Armus et al. 2007), and the present sample were derived the same way. Brandl et al. (2006) used a different method to derive the same parameters; their method would give lower 7.7 μm PAH flux densities and luminosities. This is due to the complicated continuum at $\sim$8 μm. Our 11.3 μm PAH flux densities are consistent with theirs. Table 3 gives the results.

4. MULTI-WAVELENGTH STUDIES OF ULIRGS AT $z \sim 1.9$

AEGIS (Davis et al. 2007) and Far-Infrared Deep Extragalactic survey Legacy (FIDEL; Dickinson et al. 2007) provide a rich X-ray to radio data set to study the ULIRG SEDs. Objects in our sample are measured at many key bands: all are detected in all four IRAC bands (Barmby et al. 2008), all but two by *AKARI* at 15 μm (M. Im et al. 2009, in preparation), and all at 1.4 GHz (Ivison et al. 2007). Most are also detected at 70 and 160 μm in the FIDEL survey (Dickinson et al. 2007). Only two objects, EGS14 and EGS_b2, are detected in the *Chandra* 200 ks X-ray imaging (Laird et al. 2008). The flux densities in these key bands trace stellar mass, SFR, and AGN activity. Objects in the present sample were also observed with MAMBO on IRAM, and most were detected at 1.2 mm (J. Younger et al. 2009, in preparation). Table 4 gives the photometry, and the UV-to-radio SEDs are shown in Figure 7.

The multi-wavelength photometry permits us to compare the present sample with the SMG population. There is a small region covered by SCUBA in EGS by Webb et al. (2003), but no galaxies in the present sample are in the SCUBA region. We fit FIR SEDs for the sample and predict their 850 μm flux densities F_{850} to be in the range $2.2 < F_{850} < 8.4$ mJy (Table 4). These values are similar to the flux densities for SMGs at the same redshifts (Chapman et al. 2005; Pope et al. 2006, 2008). The median F_{850} for this sample is 4.5 mJy, compared with the median F_{850} of 5.5 mJy for SMGs at $1.5 < z < 2.2$ found by Chapman et al. (2005) and 7.5 mJy by Pope et al. (2006, 2008). In more detail, 7 out 12 objects in the present sample have F_{850} fainter than 5 mJy, while the flux densities for most SMGs in Chapman et al. (2005) and Pope et al. (2006, 2008) are brighter than 5 mJy. We therefore argue that this sample is part of a slightly faint SMG population.

Optical and radio morphologies of the galaxies provide important information on their assembly histories. *HST* ACS F814W imaging (Lotz et al. 2008) covers the central $1^\circ \times 10'$ region of the EGS. EGS1/4/b2 are outside the ACS coverage, but rough optical morphologies are available from Subaru *R*-band images. Optical images of each object are presented with their SEDs in Figure 7. Most objects have irregular or clumpy morphologies in the rest-frame 2000Å $< \lambda <$ 3000Å bands with a typical size of 1.″5, suggesting extended star formation in a region with a size of about 13 kpc. The 1.4 GHz radio imaging of EGS has a mean circular beam width of $\sim$3.″8 FWHM (Ivison et al. 2007) and is unable to resolve morphologies except in a few cases. EGS23 and 24 show elongated radio morphologies aligned with their optical extent, indicating that the radio and rest-frame UV light are from the same extended star formation regions in both cases.

The spatial distribution of the stellar population is traced by the rest-frame optical imaging. Windhorst et al. (2002), Papovich et al. (2005), and Conselice et al. (2005) have argued that UV-dominated star-forming galaxies at high redshifts have similar morphologies in the rest-frame UV and optical bands. One outstanding property of galaxies in the present sample is their extremely red optical–NIR color. Seven objects in the sample have observed $(R - K)_{\mathrm{Vega}} > 5$, qualifying them as extremely red objects (ERO). EGS4 is the reddest with $(R - K)_{\mathrm{Vega}} = 6.8$. Red colors like these are common among distant ULIRGs; examples include ERO J164502+4626.4 (=[HR94] 10 or sometimes "HR 10") at $z = 1.44$ (Elbaz et al. 2002) and CFRS 14.1157 at $z = 1.15$ (Le Floc'h et al. 2007). EROs are

Table 4
IR/Radio Flux and Luminosity of the Sample

Object	$F(3.6\,\mu m)$ (μJy)	$F(4.5\,\mu m)$ (μJy)	$F(5.8\,\mu m)$ (μJy)	$F(8.0\,\mu m)$ (μJy)	$F(15\,\mu m)$ (μJy)	$F(24\,\mu m)$ (μJy)	$F(70\,\mu m)$ (mJy)	$F(160\,\mu m)$ (mJy)	$F(850\,\mu m)$[b] (mJy)	$F(1.1\,mm)$ (mJy)	$F(1.4$ GHz) (mJy)	L_{IR}[c] ($L_\odot$)	q
EGS1	45.0 ± 0.3	55.4 ± 0.4	63.6 ± 1.5	56.3 ± 1.6	...[d]	554 ± 35	<1.5	12.1 ± 8.9	3.3	1.86 ± 0.50	0.069 ± 0.010	12.72 ± 0.15	2.25
EGS4	32.1 ± 0.3	44.9 ± 0.4	52.1 ± 1.5	40.1 ± 1.5	125 ± 24	557 ± 22	2.4 ± 0.5	<21.0	3.9	1.87 ± 0.48	0.062 ± 0.010	12.62 ± 0.12	2.19
EGS10	21.8 ± 0.3	23.0 ± 0.3	34.0 ± 1.4	28.9 ± 1.5	77 ± 28	623 ± 35	4.2 ± 0.7	45.5 ± 8.7	5.2	1.65 ± 0.69	0.085 ± 0.014	12.83 ± 0.10	2.33
EGS11	27.8 ± 0.3	36.9 ± 0.4	38.2 ± 1.4	30.6 ± 1.5	192 ± 31	591 ± 20	5.0 ± 0.6	<21.0	3.3	0.85 ± 0.44	0.067 ± 0.017	12.58 ± 0.09	2.24
EGS12	27.7 ± 0.3	31.0 ± 0.3	38.3 ± 1.4	33.2 ± 1.5	196 ± 25	743 ± 23	3.9 ± 0.6	a	5.4	1.58 ± 0.47	0.036 ± 0.010	12.77 ± 0.07	2.59
EGS14	66.1 ± 0.2	89.6 ± 0.4	101.7 ± 1.5	88.4 ± 1.6	457 ± 39	1053 ± 41	3.8 ± 0.6	76.7 ± 9.6	6.4	4.54 ± 0.68	0.316 ± 0.023	13.18 ± 0.06	1.95
EGS21	39.5 ± 0.3	45.3 ± 0.4	50.7 ± 1.5	35.0 ± 1.5	59 ± 14	605 ± 23	2.8 ± 0.5	34.2 ± 9.4	8.4	1.31 ± 0.35	0.070 ± 0.014	13.15 ± 0.07	2.26
EGS23	47.8 ± 0.3	60.6 ± 0.4	69.1 ± 1.5	51.3 ± 1.5	132 ± 29	665 ± 18	3.7 ± 0.4	62.4 ± 8.7	4.5	1.81 ± 0.40	0.119 ± 0.015	12.79 ± 0.08	2.08
EGS24	36.4 ± 0.3	44.0 ± 0.4	46.8 ± 1.4	37.1 ± 1.5	65 ± 25	663 ± 29	3.4 ± 0.6	9.7 ± 9.0	2.7	1.49 ± 0.74	0.047 ± 0.012	12.51 ± 0.18	2.16
EGS26	31.7 ± 0.3	43.3 ± 0.4	47.1 ± 1.4	34.0 ± 1.5	58 ± 20	492 ± 16	1.5 ± 0.5	21.6 ± 8.4	4.5	1.14 ± 0.36	0.097 ± 0.017	12.49 ± 0.15	2.15
EGS24a	22.3 ± 0.3	32.3 ± 0.3	46.7 ± 1.5	575 ± 1.6	223 ± 36	997 ± 30	2.5 ± 0.5	15.1 ± 8.4	6.4	2.87 ± 0.54	0.112 ± 0.013	12.91 ± 0.10	1.91
EGS_b2	94.0 ± 0.2	124.8 ± 0.4	115.0 ± 1.5	117.1 ± 1.6	...	616 ± 30	3.4 ± 0.5	21.7 ± 7.0	2.2	...	0.151 ± 0.009	12.34 ± 0.14	1.80

Notes.
[a] Confused.
[b] Prediction from the SED fitting.
[c] FIR luminosity of the best-fit CE03 template.
[d] Not observed.

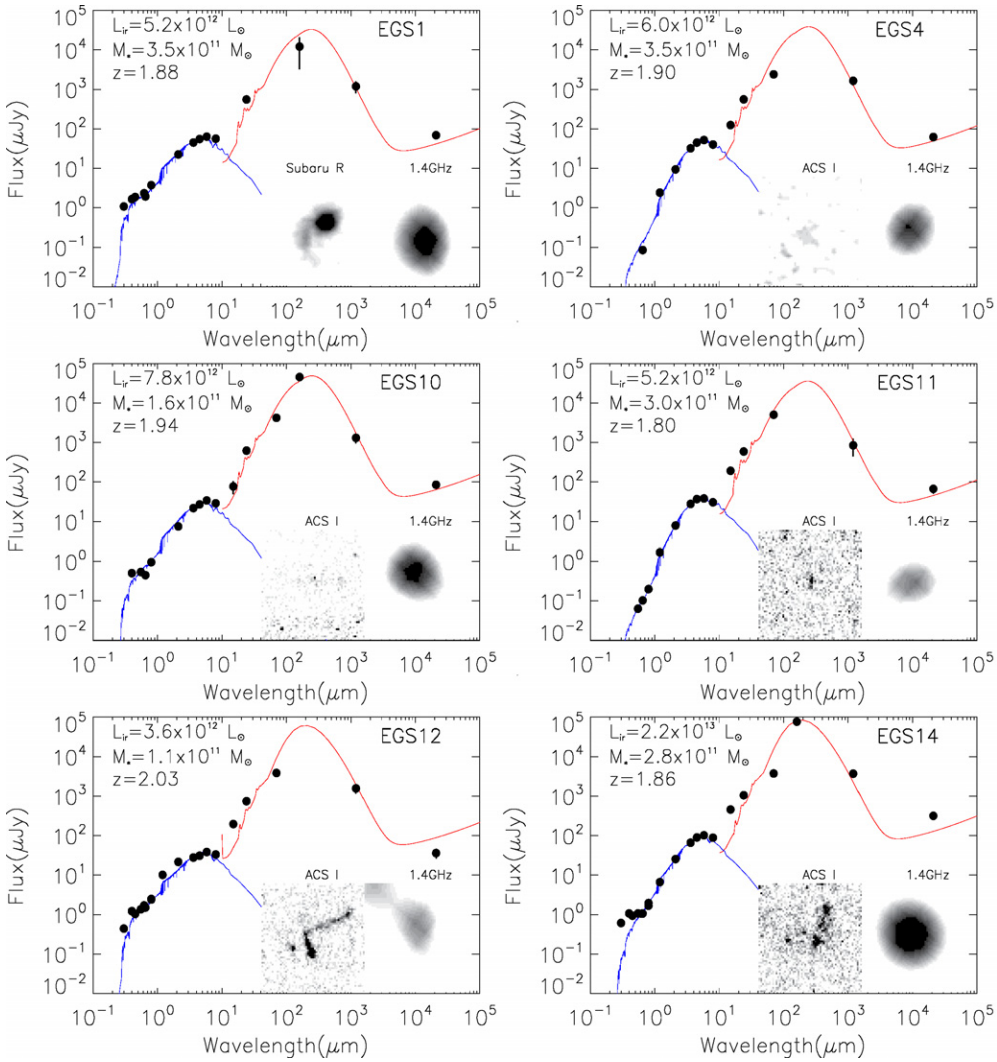

Figure 7. Spectral energy distributions and morphologies for sample galaxies. Inset images are in negative grayscale and are 12″ square. The red images come from *HST* ACS data (filter F814W) if available; otherwise Subaru *R*. the black dots represent photometric data, and the blue line is the stellar population model (BC03) that best fits each source. The red lines are the CE01 dust templates chosen to match the FIR luminosity of each source.

(A color version of this figure is available in the online journal.)

commonly seen as counterparts to SMGs (Smail et al. 1999; Frayer et al. 2004). The red optical–NIR colors, corresponding to rest NUV−R for our sample, indicate either dust extinction in these objects or high stellar mass. The stellar population modeling in the next paragraph suggests that objects in our sample have both heavy dust extinction and high stellar masses. The heavy dust extinction does not seem to reconcile with objects being detected in the ACS 606W and 814W bands, which are the rest-frame 1800–2600Å for galaxies at $z \sim 2$. The irregular and clumpy morphologies in Figure 7 are highly non-uniform dust extinction in the objects in our sample. Only two objects are undetected in the deep ACS 814W image, probably due to higher column density of dust in the compact stellar and gas distribution.

4.1. Stellar Population and Mass in ULIRGs

Stellar population modeling provides a way of determining physical parameters from the observational data, but it is very difficult to model stellar populations in ULIRGs. Tacconi et al. (2002) measured dynamical masses for a sample of local ULIRGs with NIR spectroscopy and found stellar masses in the range of $3 \times 10^{10}\ M_\odot < M_* < 2.4 \times 10^{11}\ M_\odot$ with a mean of $1.1 \times 10^{11}\ M_\odot$. Their local sample has a mean absolute K-band magnitude of $M_K = -25.8$ after adopting a dust correction of $A_K = 0.7$ mag. The IRAC 8 μm flux densities of this sample correspond to a similar K-band magnitude range with $\langle M_K \rangle = -25.7$ if the same dust correction is used. This suggests a similar mass range for our sample, $M_* \sim 10^{11}\ M_\odot$.

ULIRGs have a burst star formation history, very young stellar populations, and non-uniform dust distribution, all of which can introduce large uncertainties in modeling their stellar populations. On the other hand, stellar masses are the most robust property against variations in star formation history, metallicities, and extinction law in modeling stellar population (Förster Schreiber et al. 2004). We perform a stellar population analysis on the present sample, mainly to measure their stellar masses. We fit galaxy SEDs with Bruzual & Charlot et al. (2003, hereafter BC03) stellar population models with a Salpeter IMF and a constant SFR. Several groups (Shapley et al. 2001; van Dokkum et al. 2004; Rigopoulou et al. 2006; Lai et al. 2007) have argued that a constant SFR provides a reasonable description

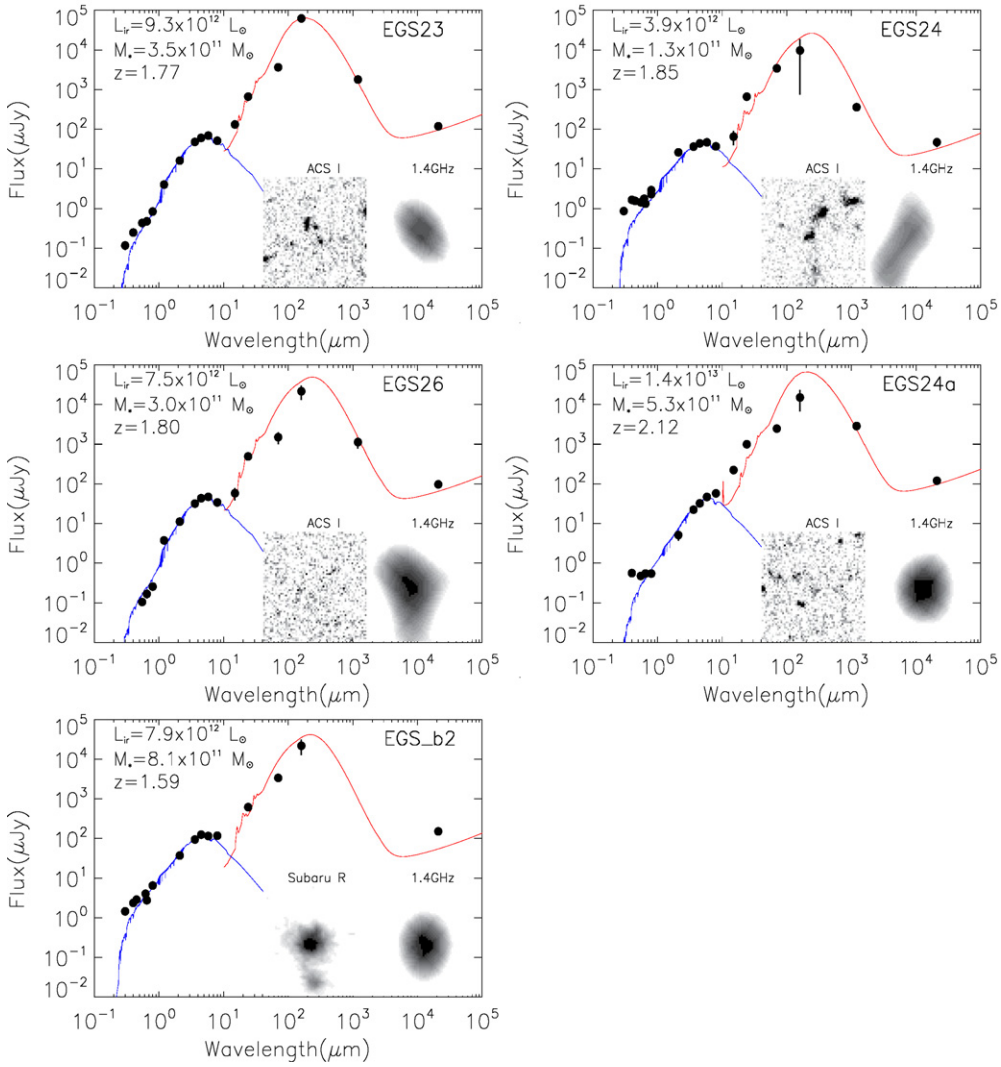

Figure 7. (Continued)
(A color version of this figure is available in the online journal.)

of stellar population evolution for galaxies with ongoing star formation at high redshifts, such as LBGs, Lyman-alpha emitters (LAEs), and DRGs. The stellar population age, dust reddening $E(B-V)$, stellar mass, and derived SFR from the model fitting are listed in Table 5, and the model SED fits are shown in Figure 7. Objects in this sample have estimated stellar masses with $M_* > 10^{11}\ M_\odot$, similar to values found for local ULIRGs (Tacconi et al. 2002), DRGs, and *BzK* galaxies (Labbe et al. 2005; Daddi et al. 2007b).

4.2. Total Infrared Luminosity and Star Formation Rate

Two of the most-popular methods of estimating SFRs of local galaxies use total infrared luminosity $L_{\rm IR}$ and radio luminosity $L_{1.4\ \rm GHz}$ (Condon 1992; Kennicutt 1998). The validity of these methods needs to be established at high redshift. Most objects in the present sample are detected at 70 μm, 160 μm, and 1.2 mm, permitting a direct measurement of total infrared luminosity $L_{\rm IR}$ (Papovich et al. 2007). In practice, we derived $L_{\rm IR}$ by fitting SED templates (Chary & Elbaz 2001) to the observed 70 μm, 160 μm, and 1.2 mm flux densities (Figure 7). All galaxies in the sample have $L_{\rm IR} > 10^{12}\ L_\odot$ (Table 4), qualifying them as ULIRGs. EGS14 and EGS21 have $L_{\rm IR} > 10^{13}\ L_\odot$ and are thus HyperLIRGs. All sample galaxies are also detected at 1.4 GHz (Ivison et al. 2007). We will be able to verify (1) whether $L_{1.4\ \rm GHz}$ is correlated with $L_{\rm IR}$ for ULIRGs at $z \sim 2$, and (2) whether such a correlation at high redshifts is consistent with the local one (Condon 1992). Figure 8 plots the radio luminosity $L_{1.4\ \rm GHz}$ versus $L_{\rm IR}$ for this sample and variety of local SB and ULIRG samples. The FIR–radio ratios q for this sample[26] are in Table 4 with a mean $\langle q\rangle = 2.19 \pm 0.20$. Kovacs et al. (2006) measured $L_{\rm IR}$ using 350 μm, 850 μm, and 1.2 mm flux densities and obtained a mean $\langle q\rangle = 2.07 \pm 0.3$ for SMGs at $1 < z < 3$. Both measurements yield q for ULIRGs at $z \sim 2$ close to, but smaller than the local value $q = 2.36$. Sajina et al. (2008) showed more clearly a trend in their AGN-dominated sample at $z \sim 2$: sources with strong PAH emission have q in $1.6 < q < 2.36$; while all power-law sources have $q < 1.6$. Normally, radio excess is due to non-thermal emission from AGNs, but galaxy merging can also enhance the non-thermal synchrotron radiation (Condon 1992). Merging processes are evident in our sample. We will argue in following paragraphs that AGNs activities may exist in most objects in the sample. In fact, two X-ray sources, EGS14 and EGS_b2, and the serendipitous power-law source EGS24a show higher radio excess (lower q) than rest objects in

[26] $q = \log(\frac{F_{\rm FIR}}{3.75^{12}\ \rm Wm^{-2}}) - \log(\frac{F_{1.4\ \rm GHz}}{\rm Wm^{-2}Hz^{-1}})$ defined by Condon (1992).

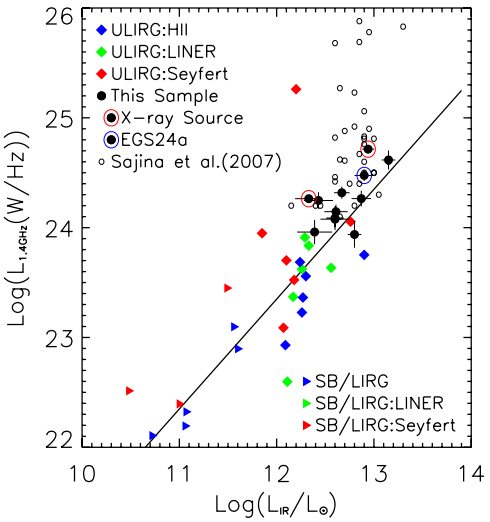

Figure 8. Correlation between $L_{\rm IR}$ and $L_{1.4\,\rm GHz}$. $L_{\rm IR}$ was calculated by fitting SED templates (CE01) to the MIPS 70, 160 μm, and MAMBO 1.2 mm photometry. The two points with red circles are the X-ray sources EGS14 and EGS_b2, and the one with a blue circle is the serendipitous object EGS24a. The sample is plotted together with local starburst (SB) galaxies and ULIRGs against the local FIR–radio relation (the thick line, Condon, 1992). The color coding: Seyferts in the local ULIRG and SB samples are shown in red; LINERs in the local ULIRG and SB samples are shown in green; and SB/HII-type ULIRGs in blue, the same as in Figure 6. This plot shows that the local SB galaxies and ULIRGs, and objects in our sample are all consistent with the local FIR–radio relation (Condon, 1992). Objects in Sajina et al. (2007a) show strong radio excesses indicating AGNs in their sample.

(A color version of this figure is available in the online journal.)

Table 5
Stellar Population Fitting Parameters

Name	Age (Gyr)	$E(B-V)$	M_* 10^{11} ($M_\odot$)	SFR ($M_\odot$ yr^{-1})
EGS1	1.9	0.3	5	240
EGS4	1.4	0.7	5	320
EGS10	1.1	0.4	2	182
EGS11	2.0	0.7	4	196
EGS12	0.29	0.4	1	480
EGS14[a]	0.26	0.6	3	1320
EGS23	1.1	0.6	5	400
EGS24	0.29	0.5	5	580
EGS26	1.8	0.6	4	220
EGS_b2[a]	0.03	0.6	0.9	3800

Notes. EGS24a, the serendipitous object next to EGS24, was not fitted with any model because it has a power-law SED in the IRAC bands.
[a] EGS14 and EGS_b2 are X-ray sources, and their SEDs may be contaminated by AGNs.

the sample. Two scenarios can be differentiated by their radio morphologies: AGNs are point sources and mergers, in most cases, are extended sources. Currently, we cannot determine which scenario is responsible to the radio excess due to lower resolution of the 1.4 GHz radio images (Figure 7).

Another measure used to estimate $L_{\rm IR}$ for local galaxies is the IRAC 8 μm luminosity, $L_{8\,\mu\rm m}$, though there is considerable debate about how reliable this method is. $L_{8\,\mu\rm m}$ is defined as $L_{8\,\mu\rm m} = 4\pi d_L^2(\nu F_\nu)_{8\,\mu\rm m}$ where F_ν is the rest-frame IRAC 8 μm flux density (Huang et al. 2007b). $L_{8\,\mu\rm m}$ is found to be correlated with $L_{\rm IR}$ for local galaxies (Wu et al. 2005). The MIPS 24 μm band directly measures the rest IRAC 8 μm flux densities for our sample. A galaxy's 8 μm flux density actually has two

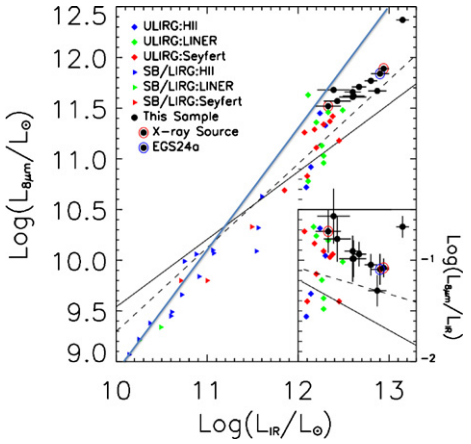

Figure 9. Rest-frame 8 μm luminosity, $L_{8\,\mu\rm m}$ vs. total infrared luminosity, $L_{\rm IR}$. ULIRGs in this sample are shown as filled black dots; the two points with red circles are the X-ray sources EGS14 and EGS_b2, and the one with a blue circle is the serendipitous object EGS24a; local starburst (SB) galaxies as triangles, and local ULIRGs as diamonds. Local SBs and ULIRGs are color coded based on their spectral classification (Veilleux et al. 1995, 1999; Brandl et al. 2006): red for Seyfert, green for LINER, and blue for H II/SB. Two template models (Daddi et al. 2007b) and one empirical (Bavouzet et al. 2008) are also plotted: DH02 models as the dashed line, CE01 models as the solid line, and the empirical model as blue solid line. The inset shows the same data for the high-luminosity galaxies but plotted as the *ratio* of $L_{8\,\mu\rm m}/L_{\rm IR}$. $L_{8\,\mu\rm m}$ was measured for each galaxy by convolving its spectrum with the redshifted bandpass of the IRAC 8 μm filter. In this plot, rest-frame 8 μm luminosities for the present sample are correlated with their total infrared luminosities, but the observed $L_{8\,\mu\rm m}$–$L_{\rm IR}$ relation is higher than both CE01 and DH02 model predictions. This implies that both models will overestimate the $L_{\rm IR}$ for the present sample based on their $L_{8\,\mu\rm m}$.

(A color version of this figure is available in the online journal.)

components (aside from starlight, which can be subtracted if necessary): the 7.7 μm PAH emission feature complex and a featureless continuum, coming from an AGN or warm dust in the interstellar medium. There are several models for the IR emission from galaxies, which convert $L_{8\,\mu\rm m}$ to $L_{\rm IR}$ (Chary & Elbaz 2001; Dale & Helou 2002, hereafter CE01 and DH02). Empirically, Wu et al. (2005) and Bavouzet et al. (2008) found a correlation between $L_{8\,\mu\rm m}$ and both $L_{1.4\,\rm GHz}$ and $L_{\rm IR}$ for star-forming galaxies. At the high-luminosity end, local ULIRGs deviate from this correlation with higher $L_{8\,\mu\rm m}/L_{\rm IR}$ ratios, such a trend was also see by Rigby et al. (2008).

Figure 9 shows a correlation between $L_{8\,\mu\rm m}$ and $L_{\rm IR}$ for all populations. However, the $L_{8\,\mu\rm m}$–$L_{\rm IR}$ relation for objects in our sample and the local ULIRGs with high $L_{\rm IR}$ has a higher offset than that for the local SB galaxies and the model prediction (Chary & Elbaz 2001; Dale & Helou 2002). This indicates that, for a given $L_{\rm IR}$, $L_{8\,\mu\rm m}$ for objects in our sample and some of local ULIRGs is higher than the model prediction. Thus, objects in our sample have an 8 μm excess comparing with the CE01 and DH02 model prediction. The empirical $L_{8\,\mu\rm m}$–$L_{\rm IR}$ relation of Bavouzet et al. (2008) derived with samples at various redshifts matches local SB galaxies, but predicts much high $L_{8\,\mu\rm m}$ for ULIRGs and HyperLIRGs. The $L_{8\,\mu\rm m}$–$L_{\rm IR}$ relation for our sample permits to estimate $L_{\rm IR}$ for same type of objects with only 24 μm flux densities.

Our IRS spectra can be used to separate the PAH from continuum in the (rest) 8 μm band, and each component's contribution to $L_{8\,\mu\rm m}$ can be measured. PAH luminosity is thought to be a generally good tracer of SFR, but the $L_{7.7\,\mu\rm m}/L_{\rm IR}$ ratio is known to be luminosity dependent, decreasing at high luminosity (Rigopoulou et al. 1999; Desai et al. 2007; Shi et al.

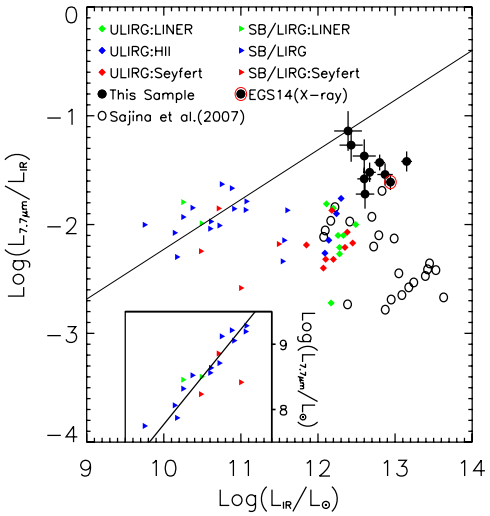

Figure 10. 7.7 μm PAH to total infrared luminosity ratio vs. total infrared luminosity. The $L_{7.7}/L_{\rm IR}$ ratio measures the star formation contribution in the total infrared luminosity for objects in the sample. The present sample has the highest $L_{7.7}/L_{\rm IR}$ ratio, indicating that they are starburst (SB)-dominated ULIRGs. The $L_{7.7}/L_{\rm IR}$ ratio for the present sample is still compatible to the empirical relation of $L_{7.7}/L_{\rm IR} \sim L_{\rm IR}^{0.45}$ from the local SB galaxies. Objects in the present sample are shown as filled black dots (the X-ray source EGS14 is a filled dots with red circle, the 7.7 μm PAH in the other X-ray sources EGS_b2 is not in our observation band, thus it is not in the diagram); local SB galaxies as triangles, and local ULIRGs as diamonds. Local SBs and ULIRGs are color coded based on their spectral classification (Veilleux et al. 1995, 1999; Brandl et al. 2006): red for Seyfert, green for LINER, and blue for H II/SB. The open circles show ULIRGs and HyperLIRGs from the Yan et al. (2005) sample with data from Sajina et al. (2007a). The inserted plot shows a strong correlation between $L_{7.7}$ and $L_{\rm IR}$ for the local SB galaxies. The thick lines show linear fits to the correlations for local SB galaxies as $L_{\rm IR} \sim L_{7.7}^{0.69}$, which transfers to $L_{7.7}/L_{\rm IR} \sim L_{\rm IR}^{0.45}$ plotted with the thick line.
(A color version of this figure is available in the online journal.)

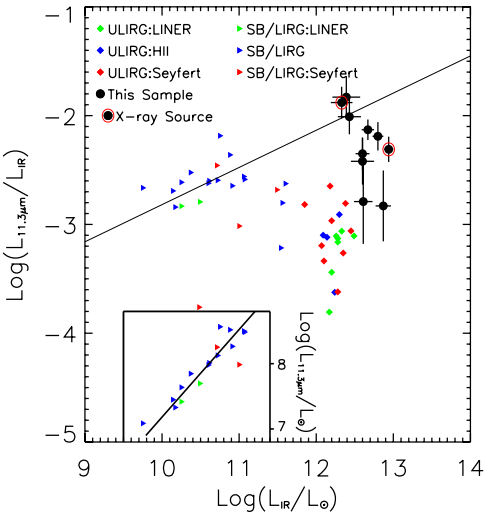

Figure 11. 11.3 μm PAH to total infrared luminosity ratio vs. total infrared luminosity. The plot shows the same pattern as in Figure 10. Objects in the present sample are shown as filled black dots; the two filled dots with red circles are two X-ray sources, EGS14 and EGS_b2; local starburst (SB) galaxies as triangles, and local ULIRGs as diamonds. Local SBs and ULIRGs are color coded based on their spectral classification (Veilleux et al. 1995, 1999; Brandl et al. 2006): red for Seyfert, green for LINER, and blue for H II/SB. The inserted plot shows a strong correlation between $L_{11.3}$ and $L_{\rm IR}$ for the local SB galaxies. The thick lines show linear fits to the correlations for local SB galaxies as $L_{\rm IR} \sim L_{11.3}^{0.75}$, which transfers to $L_{11.5}/L_{\rm IR} \sim L_{\rm IR}^{0.33}$ plotted with the thick line.
(A color version of this figure is available in the online journal.)

2007). Figure 10 shows $L_{7.7\ \mu{\rm m}}/L_{\rm IR}$ versus $L_{\rm IR}$. In this diagram, each population is well separated from the others. The average $L_{7.7\ \mu{\rm m}}/L_{\rm IR}$ ratio for local ULIRGs is seen to be lower than for local SB galaxies. The HyperLIRGs in Yan et al. (2005) and Sajina et al. (2007a) have the lowest $L_{7.7\ \mu{\rm m}}/L_{\rm IR}$ ratio. In contrast, the present sample has the highest $L_{\rm PAH}/L_{\rm IR}$ ratio, and the trend is the same for the 11.3 μm PAH feature (Figure 11). Objects with such a high PAH luminosity have neither been found locally nor in the MIPS 24 μm-luminous sample at $z \sim 2$ (Yan et al. 2005; Houck et al. 2005).

SB galaxies were expected to have the highest $L_{\rm PAH}/L_{\rm IR}$, and $L_{\rm PAH}/L_{\rm IR}$ was seen to decrease with increasing $L_{\rm IR}$. Our sample shows a new ULIRG population with much higher PAH emissions at 7.7 and 11.3 μm. We argue that the high $L_{\rm PAH}/L_{\rm IR}$ ratio for our sample is generally compatible to extrapolation from the $L_{\rm PAH}/L_{IR}$–$L_{\rm IR}$ relation for SB galaxies. Both $L_{7.7\ \mu{\rm m}}$ and $L_{11.3\ \mu{\rm m}}$ for local SB galaxies are strongly correlated with $L_{\rm IR}$ in Figures 10 and 11. We fit both data sets and obtain the following relations: $L_{\rm IR} \propto (L_{7.7\ \mu{\rm m}})^{0.69}$ and $L_{\rm IR} \propto (L_{11.3\ \mu{\rm m}})^{0.75}$. Both relations convert to $L_{7.7\ \mu{\rm m}}/L_{\rm IR} \propto (L_{\rm IR})^{0.45}$ and $L_{11.3\ \mu{\rm m}}/L_{\rm IR} \propto (L_{\rm IR})^{0.33}$, respectively, as plotted in Figures 10 and 11. The $L_{\rm PAH}$–$L_{\rm IR}$ relation for local SBs predicts a higher $L_{\rm PAH}$–$L_{\rm IR}$ ratio in the $L_{\rm IR}$ range for our sample. Our samples have high $L_{\rm PAH}$–$L_{\rm IR}$ ratio close to the extrapolation comparing with other ULIRGs population, indicating a SB domination. The deficient PAH emission in our sample implies most likely existence of AGN in our sample, though strong UV from intensive star-forming region can also destroy PAH.

Table 6
Comparison of Star Formation Rates

Name	SFR (BC03)[a] ($M_\odot$ yr^{-1})	SFR (7.7)[b]	SFR (11.3)[b]	SFR ($L_{\rm IR}$)[c]
EGS1	240	386 ± 18	263 ± 68	945 ± 326
EGS4	320	226 ± 21	142 ± 90	750 ± 207
EGS10	182	452 ± 14	207 ± 110	1217 ± 280
EGS11	196	277 ± 21	297 ± 61	684 ± 142
EGS12	480	481 ± 15	549 ± 103	1060 ± 171
EGS14	1320	451 ± 28	568 ± 97	2724 ± 376
EGS23	400	340 ± 21	487 ± 42	1110 ± 204
EGS24	580	398 ± 19	504 ± 60	582 ± 241
EGS26	220	346 ± 16	390 ± 41	556 ± 192
EGS_b2	3800	...	417 ± 29	394 ± 127

Notes.
[a] Star formation rate (SFR) calculated from stellar population model (BC03) fitting.
[b] SSFR calculated from PAH feature luminosity.
[c] SFR calculated from far infrared luminosity $L_{\rm IR}$.

The MIR spectral properties and $L_{\rm PAH}/L_{\rm IR}$ of our sample are closer to local SB galaxies, even though their $L_{\rm IR}$ differs by 2 orders of magnitude. Farrah et al. (2007) reached the same conclusion by comparing silicate absorption strength for their sample with those for local ULIRG and SB galaxies, and they propose six possible scenarios to explain the similarity between high-redshift ULIRGs and local SB galaxies. Our multi-wavelength data set provides further constrain on physical properties of our sample. The ACS *I*-band images (Figure 7) show multi-clumpy morphologies extended to >10 Kpc size for most objects in our sample. At $z \sim 2$, the observed *I* band probes the rest NUV band, thus is sensitive to star formation. Local ULIRGs, however, have much more compact morphologies

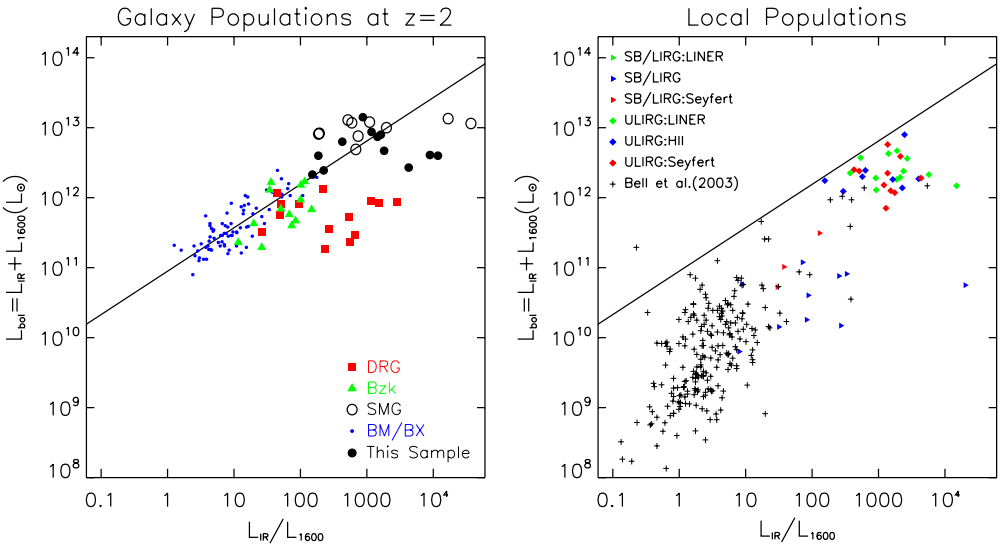

Figure 12. IR-to-UV luminosity ratio for galaxies at $z \sim 2$ and $z \sim 0$. The left panel is for galaxies at $z \sim 2$. Our sample is plotted against galaxies at $z \sim 2$ selected in various bands. The solid lines in both panels are the $L_{\rm IR}/L_{1600}$–$L_{\rm IR} + L_{1600}$ relation for BM/BX sources, *BzK* galaxies, DRGs, and SMGs (Reddy et al. 2006). The right panel is for local galaxies including normal galaxies (Bell et al. 2005), starburst galaxies (Brandl et al. 2006), and ULIRGs. Most objects in our sample have the same relation as the rest of galaxies population at $z \sim 2$. Three objects in our sample with extreme red colors, together with some DRGs in Reddy et al. (2006), are off the relation. They locate in the region where local ULIRGs are, indicating a compact dust distribution in those objects. See detailed discussion in the text.

(A color version of this figure is available in the online journal.)

in the *Galaxy Evolution Explorer* (*GALEX*) NUV images.[27] The extend morphologies of our sample support both gas-rich merging and SB geometry scenarios proposed by Farrah et al. (2007). In this scenario, the silicate dust column density is reduced after star formation region is stretched to a large-scale during merging. The extended morphologies in rest NUV indicate an extended star formation in our sample, thus extended distribution of PAH emission. In such an extended distribution, more PAH can survive in strong UV radiation field from central AGN than those in a compact distribution. This scenario thus explains the higher $L_{\rm PAH}/L_{\rm IR}$ in our sample than local ULIRGs.

Star-forming galaxies at $z \sim 2$ are found to generally have much less dust extinction than their local counterparts. Reddy et al. (2006) found that there is a correlation between $L_{\rm IR}/L_{1600}$ and $L_{1600} + L_{\rm IR}$ for star-forming galaxies at $z \sim 2$, where L_{1600} is the monolithic luminosity at 1600 Å. This correlation has a higher offset than the local relation, indicating less dust extinction in the line of sight for galaxies at $z \sim 2$. Most objects in our sample lie upon the $L_{1600}/L_{\rm IR}$–$L_{1600} + L_{\rm IR}$ relation for galaxies $z \sim 2$ (Figure 12). Reddy et al. (2006) argued that dust distribution and star formation region become more compact in local galaxies. We argue that lower surface density of dust density and extended star formation region with high SFR permit to detect both UV and PAH emission from most objects in ours sample.

The SFR for a galaxy can be estimated from its FIR and UV emission. Specifically, SFR is given as (Kennicutt 1998; Bell et al. 2005)

$$\mathrm{SFR}/(M_\odot\ \mathrm{yr}^{-1}) = C \times (L_{\rm IR} + 3.3L_{280})/L_\odot, \qquad (3)$$

where L_{280} is the monochromatic luminosity (uncorrected for dust extinction) at rest-frame 280 nm (Wolf et al. 2005). The constant C is 1.8×10^{-10} for the Salpeter IMF (Kennicutt 1998), and 9.8×10^{-11} for the Kroupa IMF (Bell et al. 2005). In the following text, we will adopt the Salpeter IMF for all $L_{\rm IR}$–SFR conversion in this paper. SFR will reduce by a factor of ~2 if we switch to the Kroupa IMF (Bell et al. 2005). The 280 nm band shifts to the observed *I* band at $z \approx 2$. L_{280} was calculated from the ACS F814W magnitude if available or otherwise the CFHT *I* magnitude. All objects in our sample have L_{280} in the range $5 \times 10^8 < L_{280} < 3 \times 10^{10}\ L_\odot$, less than 1% of their $L_{\rm IR}$. The SFR seen at rest-frame 280 nm is at most 20 $M_\odot\ \mathrm{yr}^{-1}$, and most UV light produced by newborn stars is absorbed by dust and re-emitted in the infrared. Thus, we omit the L_{280} contribution in our SFR calculation. The SFRs calculated with $L_{\rm IR}$, $L_{\rm PAH}$, and the stellar synthesis model are in Table 6.

Total infrared luminosity, $L_{\rm IR}$, of ULIRGs may be partly powered by AGNs (Nardini et al. 2008), thus using $L_{\rm IR}$ may overestimate their SFR. The PAH emission only traces star formation, and is free of AGN contamination. We calculate SFR for our sample with their $L_{\rm PAH}$ using the $L_{\rm PAH}$–SFR relation, established from local SB galaxies shown in Figures 10 and 11. Results are given in Table 5. SFRs for our sample converted from $L_{\rm IR}$ using Equation (3) are much higher, with an average SFR $\sim$ 1000 $M_\odot\ \mathrm{yr}^{-1}$. $L_{7.7\,\mu\mathrm{m}}$ and $L_{11.3\,\mu\mathrm{m}}$ (Table 5) give smaller, SFRs, in the range $150 < \mathrm{SFR} < 600\ M_\odot\ \mathrm{yr}^{-1}$ for most objects that are quite consistent with the stellar population modeling results. The discrepancy between both star formation estimations may be due to (1) part of star formation occurs in region with no PAH, thus $L_{\rm PAH}$ underestimates the SFR, (2) $L_{\rm IR}$ contains AGN contribution, thus overestimates the SFR. It is very possible that both can happen in one object simultaneously, namely, its AGN destroys PAH in surrounding area where star formation occurs. This will further increase the discrepancy, so the real SFR should be in between both estimations (Table 6).

Our sample have both high SFR and high stellar mass, supporting the galaxy formation in the "downsizing" mode. The SFRs and stellar masses for our sample are consistent with the SFR–stellar-mass relation obtained from *BzK* galaxies at

[27] The *GALEX* UV morphologies for local SB galaxies and local ULIRGs are from http://galex.stsci.edu/GalexView/

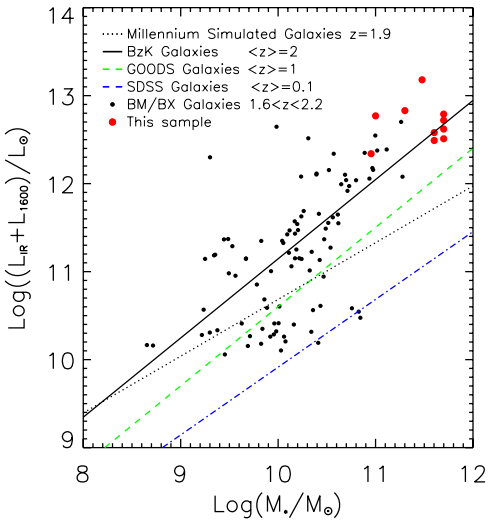

Figure 13. SFR–stellar-mass relation for galaxies at $z = 0$, 1, and 2 suggests the "downsizing" scenario for galaxy formation. The mean $L_{\rm IR}$–M_* relation for *BzK* at $z \sim 2$ is from Daddi et al. (2007b), the relations for GOODS galaxies at $z \sim 1$ and SDSS galaxies at $z \sim 0.1$ are from Elbaz et al. (2007). Again, objects in our sample are consistent with the relation for BM/BX sources and *BzK*, but at high-mass end. Both simulated galaxy population models of Kitzbichler & White (2007) and Cattaneo et al. (2008) predict much lower star formation rate for galaxies with a given stellar mass.

(A color version of this figure is available in the online journal.)

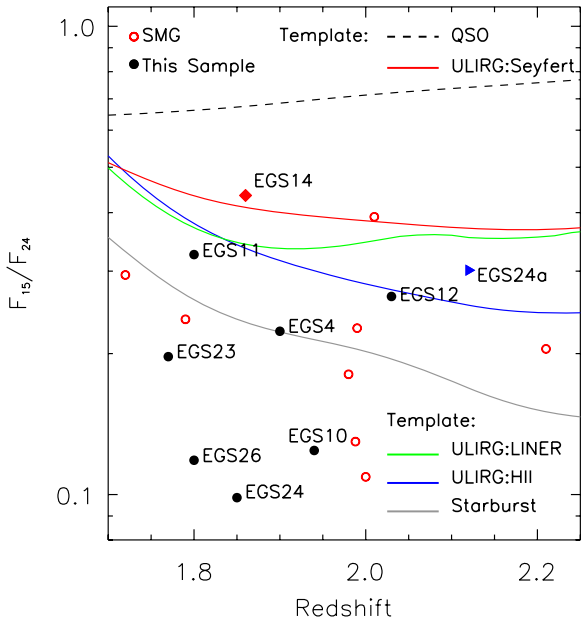

Figure 14. $F(15\ \mu{\rm m})/F(24\ \mu{\rm m})$ vs. redshifts for the ULIRG sample (filled circles). The SMGs from Pope et al. (2008) are also plotted (red open circles). This ratio should measure the continuum (hot dust) to PAH ratio for objects in this redshift ranger and hence the AGN contribution to the mid-IR luminosity. Lines show the relations defined by local templates (Figure 6): starburst (SB) galaxies (gray), Seyfert-type ULIRGs (red), LINER-type ULIRGs (green), H II/SB ULIRGs (blue), PG QSO (dashed line). One X-ray source, EGS_b2, is outside the *AKARI* 15 μm coverage and not plotted. The other X-ray source, EGS14 (red diamond), and the serendipitous object, EGS24a (blue triangle), have colors consistent with AGN. The 16 μm flux densities for SMGs are measured from the IRS peak-up imaging. Since the IRS 16 μm peak-up filter profile is very similar to the *AKARI* 15 μm filter profile, no correction is applied to the IRS 16 μm flux densities for SMGs.

(A color version of this figure is available in the online journal.)

$z \sim 2$ (Figure 13). Daddi et al. (2007b) showed that simulated galaxy populations taken from the Milllennium Simulation light cones of Kitzbichler & White (2007) and Cattaneo et al. (2008) failed to re-produce the SFR–star mass relation at $z = 2$, thus underestimate number of ULIRGs at $z \sim 2$.

It has been long anticipated that ULIRGs have a dominant contribution to the total infrared luminosity density, thus SFR density, at $z \sim 2$ (Le Floc'h et al. 2005). We use the $V_{\rm max}$ method to calculate the total infrared luminosity density for our sample to be $2.6 \times 10^7\ L_\odot\ {\rm Mpc}^{-3}$. The sample of Farrah et al. (2007) with the same limiting flux yields a density of $8.8 \times 10^6\ L_\odot\ {\rm Mpc}^{-3}$. We argue that the difference is due to the cosmic variance, because these objects are massive galaxies and thus have a much stronger spatial correlation. Both densities are lower than ULIRG $L_{\rm IR}$ density at $z \sim 1$, $\sim 10^8\ L_\odot\ {\rm Mpc}^{-3}$ for all ULIRGs (Le Floc'h et al. 2005). Most objects in our sample and those of Farrah et al. (2007) have $L_{\rm IR} > 5 \times 10^{12}\ L_\odot$, the major contribution to the $L_{\rm IR}$ density at $z \sim 2$ comes from ULIRGs with $10^{12} < L_{\rm IR} < 5 \times 10^{12}\ L_\odot$ (J. Huang et al. 2009, in preparation).

4.3. AGN in the $z \sim 1.9$ ULIRG Sample

One direct way of identifying an object as an AGN is to measure its X-ray luminosity. Two objects in the sample, EGS14 and EGS_b2, are in the main AEGIS-X catalog from the *Chandra* 200 ks images (Nandra et al. 2008; Laird et al. 2008). Their X-ray fluxes $F_{0.5-10\ {\rm keV}}$ are 1.2×10^{-15} and 6.4×10^{-15} erg cm^{-2} s^{-1}, respectively. Calculated X-ray luminosities L_X (Nandra et al. 2008; Georgakakis et al. 2007) are 1.0×10^{43} erg s^{-1} for EGS14 and 9.4×10^{43} erg s^{-1} for EGS_b2. Hardness ratios are 0.45 and -0.30, respectively. Therefore, EGS14 is a type 2 (obscured) AGN, and EGS_b2 is very close to a type 1 (unobscured) QSO according to the X-ray luminosity and hardness ratios (Szokoly et al. 2004). In addition to EGS14 and EGS_b2, EGS1 has a low-significance X-ray counterpart. At the location of this source, there were 6.5 net soft band counts (10 counts total with an estimated 3.5 count background). This gives a Poisson probability of a false detection of 3.5×10^{-3}. The source was not detected in the hard band. If the detection is real, EGS1 has $F_{0.5-2\ {\rm keV}} = 3.0 \times 10^{-16}$ erg cm^{-2} s^{-1} with $L_{2-10\ {\rm keV}} = 1.1 \times 10^{43}$ erg s^{-1}, thus is qualified to be an AGN.

The remaining 10 ULIRGs are not detected in the current *Chandra* observation. Stacking in the soft band gives 19.5 counts above an average background of 9.85, corresponding to $F_{0.5-2\ {\rm keV}} = 3.8 \times 10^{-17}$ erg cm^{-2} s^{-1} or $L_X = 1.1 \times 10^{42}$ erg s^{-1} at 2σ significance. There was no detection in the hard band. Even if EGS1 is added to the stacking, nothing shows up in the hard band, but the soft band detection significance rises to 3.2σ. The mean flux is $F_{0.5-2\ {\rm keV}} = 4.7 \times 10^{-17}$ erg cm^{-2} s^{-1} or $L_X = 1.3 \times 10^{42}$ erg s^{-1}. This average X-ray luminosity represents either a very weak AGN or strong star formation. Using the relation of Ranalli et al. (2003), this average X-ray luminosity corresponds to a SFR of 220 $M_\odot$ yr^{-1}, consistent with the SED and PAH estimation. However, we argue that the stacked X-ray signal comes from central point sources. These objects have very extended and elongated morphologies in the rest-frame NUV band. If the X-ray photons are from these star formation regions, stacking would not yield any signal unless they are aligned.

Emission in the rest 3–6 μm wavelength range is another indicator of AGN activity (Carleton et al. 1987; Shi et al. 2005; Alonso-Herrero et al. 2006; Hines et al. 2007; Jiang et al. 2006; Shi et al. 2007). The longer end of that range, which has minimal stellar and PAH emission contamination, is ideal for detecting what is nowadays thought to be hot dust emission closely related

to the AGN accretion disk. Luminosity at these wavelengths (L_5) can be converted to $L_{\rm IR}$ for QSOs with the QSO SED templates (Elvis et al. 1994). *AKARI* 15 μm photometry (M. Im et al. 2009, in preparation) provides the best measurement of L_5 for our sample. All galaxies within the *AKARI* coverage are detected except EGS26, for which the 3σ limiting flux density is $F_{15} < 58$ μJy (M. Im et al. 2009, in preparation). The *AKARI* 15 μm band is wide enough to include the 6.2 μm PAH feature for objects with $1.5 < z < 2.2$, but this feature is much weaker than the 7.7 μm feature. Thus, the *AKARI* 15 μm band is a better measure of AGN emission than the MIPS 24 μm band.

In fact, the F_{15}/F_{24} ratio for our sample measures the continuum-to-PAH ratio, and thus the AGN fraction. Figure 14 shows this ratio versus redshift. The ratios for the two known AGNs with *AKARI* coverage, EGS14 and EGS24a, are very close to the expected values for Seyfert 2s. EGS11 and EGS12 are similar to expectations for H II-type ULIRGs. The flux ratios for the remaining objects in our sample show even more PAH than SBs, indicating SB domination in these objects. SMGs (Pope et al. 2008) have very similar F_{15}/F_{24} ratios as objects in the present sample, implying the same properties shared by both samples. The SMGs also show very strong PAH features in their IRS spectra. This supports the argument that most objects in the present sample are part of a SMG population, and are SB-dominated ULIRGs.

A SB-dominated ULIRG can still have a deeply dust-obscured AGN. Many current theoretical models (e.g., Mihos & Hernquist 1994, 1996; Dubinski et al. 1999; Cox et al. 2006; Hopkins et al. 2006) suggest that such a dust-obscured AGN can have a significant contribution to $L_{\rm IR}$ of a ULIRG. A study of local ULIRG IRS spectra shows that an average of 15% $L_{\rm IR}$ are from central dust-obscured AGNs (Nardini et al. 2008). Nardini et al. (2008) argued that ULIRG luminosity in $5 < \lambda < 6$ is dominated by hot dust emission from AGNs. Most objects in the present sample are detected at 15 μm, thus permit to measure their rest 5 μm luminosities, $L_{5\,\mu{\rm m}}$, which trace AGN activity. $L_{5\,\mu{\rm m}}$ for the present sample is in range of $9.9 < \log(L_{5\,\mu{\rm m}}/L_\odot) < 12.6$ (Table 4). Using $(L_{\rm IR}/L_{5\,\mu{\rm m}})_{\rm QSO} = 22.8$ from the Elvis et al. (1994) QSO SED, we calculate that such a QSO contribution is about 14% of $L_{\rm IR}$ for objects in our sample, consistent with those for local ULIRGs.

5. SUMMARY

The results for the present sample combined with others in Table 1 show that high-redshift ULIRGs have a diverse range of properties, and different selection criteria to pick out different populations. The combination of IRAC colors and MIPS 24 μm flux used here selects ULIRGs with strong 7.7 μm PAH in a rather narrow redshift range around $z \simeq 1.9$. This sample shows a SB-dominated stage in gas-rich merging powered ULIRGs at $z \sim 2$. In this stage, intensive star formation occurs in much extended region with a typical scale of $\sim$15 Kpc indicated by their ACS morphologies. Objects in this sample have higher total infrared luminosities than local ULIRGs, but the $L_{\rm PAH}/L_{\rm IR}$ ratios for the sample are higher than those of local ULIRGs. We argue that the high $L_{\rm PAH}/L_{\rm IR}$ ratio is due to the extended PAH distribution, which is less affected by strong UV emission from central AGNs. Most objects follows the same $L_{\rm IR}/L_{1600}$–$L_{\rm bol}$ relation as that for BM/BX, DRG, and *BzK* galaxies, though they are at higher luminosity end.

Stellar masses in this sample already exceed 10^{11} $M_\odot$. Most stars must have formed prior to this stage. The SFR–stellar-mass relation for this sample is also consistent with that for the rest populations at $z \sim 2$, which is much higher than the theoretical model prediction.

Only a few of the ULIRGs in our sample show direct evidence to have AGNs with either high X-ray luminosities or hot dust emission in the mid-infrared. Several pieces of evidence show weak AGNs existing in this SB-dominated ULIRG sample: systematically higher $L_{1.4\,\rm GHz}/L_{\rm IR}$ ratio than the local radio–FIR relation, and an average X-ray emission of $L_X = 1.3 \times 10^{42}$ erg s^{-1} from point sources. AGN contributes on average 15% of total infrared luminosity for our sample.

This sample presents an early stage with very intensive star formation but weak or heavily obscured AGNs. ULIRGs in other samples at similar redshift but with different selection methods (Yan et al. 2005; Sajina et al. 2007a) have higher total infrared luminosities and lower PAH luminosities, indicating increasing AGN and decreasing star formation at higher $L_{\rm IR}$.

This work is based in part on observations made with the *Spitzer Space Telescope*, which is operated by the Jet Propulsion Laboratory, California Institute of Technology under a contract with NASA. Support for this work was provided by NASA through an award issued by JPL/Caltech.

Facilities: Spitzer

REFERENCES

Alonso-Herrero, A., et al. 2006, ApJ, 640, 167
Armus, L., et al. 2007, ApJ, 656, 148
Barmby, P., et al. 2008, ApJS, 177, 431
Barnes, J., & Hernquist, L. 1996, ApJ, 471, 115
Bavouzet, N., et al. 2008, A&A, 479, 83
Bell, E., et al. 2005, ApJ, 625, 23
Blumenthal, G., et al. 1984, Nature, 311, 517
Brandl, B., et al. 2006, ApJ, 653, 1129
Bruzual, G., & Charlot, S. 2003, MNRAS, 344, 1000
Carleton, N. P., Elvis, M., Fabbiano, G., Willner, S. P., Lawrence, A., & Ward, M. 1987, ApJ, 318, 595
Cattaneo, A., et al. 2008, MNRAS, 389, 567
Chapman, S., et al. 2003, Nature, 422, 695
Chapman, S., et al. 2005, ApJ, 622, 772
Chary, R., & Elbaz, D. 2001, ApJ, 556, 562
Chiar, J. E., & Tielens, A. G. G. M. 2006, ApJ, 637, 774
Cole, S., et al. 2000, MNRAS, 319, 168
Condon, J. J. 1992, ARA&A, 30, 575
Conselice, C. 2007, ApJ, 638, 686
Conselice, C., et al. 2005, ApJ, 620, 564
Conselice, C., et al. 2007, ApJ, 660, 55
Cox, T. J., Jonsson, P., Primack, J. R., & Somerville, R. S. 2006, MNRAS, 373, 1013
Daddi, E., et al. 2007a, ApJ, 631, 13
Daddi, E., et al. 2007b, ApJ, 670, 156
Daddi, E., et al. 2007c, ApJ, 670, 173
Dale, D., & Helou, G. 2002, ApJ, 576, 159
Davis, M., et al. 2007, ApJ, 660, 1
Desai, V., et al. 2007, ApJ, 669, 810
Dey, A., et al. 2008, ApJ, 677, 943
Dickinson, M., et al. 2007, BAAS, 211, 5216
Dubinski, J., Mihos, C., & Henquest, L. 1999, ApJ, 526, 607
Eggen, O. J., et al. 1962, ApJ, 136, 748
Elbaz, D., et al. 2002, A&A, 381, 1
Elbaz, D., et al. 2007, A&A, 468, 33
Elvis, M., et al. 1994, ApJS, 95, 1
Farrah, D., et al. 2007, ApJ, 667, 149
Farrah, D., et al. 2008, ApJ, 677, 957
Förster Schreiber, N. M., et al. 2004, ApJ, 616, 40
Franx, M., et al. 2003, ApJ, 587, 79
Frayer, D., et al. 2004, AJ, 127, 728
Genzel, R., et al. 1998, ApJ, 498, 579
Genzel, R., et al. 2001, ApJ, 563, 527
Georgakakis, A., et al. 2007, ApJ, 660, L15
Glazebrook, K., et al. 2004, Nature, 430, 181

Higdon, S., et al. 2004, PASP, 116, 975
Hines, D., et al. 2007, ApJ, 641, 85
Hopkins, P., et al. 2006, ApJ, 652, 864
Houck, J., et al. 2005, ApJ, 622, L105
Huang, J., et al. 2004, ApJS, 154, 44
Huang, J., et al. 2005, ApJ, 634, 136
Huang, J., et al. 2007a, ApJ, 660, 69
Huang, J., et al. 2007b, ApJ, 664, 840
Ivison, R., et al. 2007, ApJ, 660, 77
James, P. B., et al. 1999, MNRAS, 309, 585
Jiang, L., et al. 2006, AJ, 132, 2127
Kovacs, A., et al. 2006, ApJ, 650, 592
Kennicutt, R. C. 1998, ARA&A, 36, 189
Kim, D-C., & Sanders, D. B. 1998, ApJS, 119, 41
Kim, D-C., et al. 2002, ApJS, 143, 277
Kitzbichler, M. G., & White, S. D. M. 2007, MNRAS, 376, 2
Kormendy, J., & Sanders, D. 1992, ApJ, 390, 73
Labbe, I., et al. 2005, ApJ, 624, 81
Lai, K., et al. 2007, ApJ, 655, 704
Laird, E., et al. 2008, ApJS, 180, 102
Le Floc'h, E., et al. 2005, ApJ, 632, 169
Le Floc'h, E., et al. 2007, ApJ, 660, L65
Lotz, J., et al. 2008, 672, 177
Lutz, D., et al. 2005, ApJ, 625, 83
Menendez-Delmestre, K., et al. 2007, ApJ, 655, L65
Mihos, C., & Herquist, L. 1994, ApJ, 437, 611
Mihos, C., & Herquist, L. 1996, ApJ, 464, 641
McCarthy, P., et al. 2004, ApJ, 614, 9
Nandra, K., et al. 2008, ApJ, 660, 11
Nardini, E., et al. 2008, MNRAS, 385, 130
Papovich, C., Dickinson, M., Giavalisco, M., Conselice, C. J., & Ferguson, H. C. 2005, ApJ, 631, 101
Papovich, C., et al. 2004, ApJS, 154, 70
Papovich, C., et al. 2006, ApJ, 640, 92
Papovich, C., et al. 2007, ApJ, 668, 45
Papovich, C., et al. 2008, ApJ, 676, 206
Peeters, E., Hony, S., Van Kerckhoven, C., Tielens, A. G. G. M., Allamandola, L. J., Hudgins, D. M., & Bauschlicher, C. W. 2002, A&A, 390, 1089
Pope, A., et al. 2006, MNRAS, 370, 1185
Pope, A., et al. 2008, ApJ, 675, 1171
Ranalli, P., et al. 2003, A&A, 399, 39
Reddy, N., et al. 2005, ApJ, 633, 748
Reddy, N., et al. 2006, ApJ, 653, 1004
Reddy, N., et al. 2008, ApJS, 675, 48
Rigby, J., et al. 2008, ApJ, 675, 262
Rigopoulou, et al. 1999, AJ, 118, 2625
Rigopoulou, et al. 2006, ApJ, 648, 81
Rothberg, B., & Joseph, R. D. 2004, AJ, 128, 2098
Sajina, A., et al. 2007, ApJ, 664, 713
Sajina, A., et al. 2008, ApJ, 683, 659
Sanders, D., & Mirabel, I. F. 1996, ARA&A, 34, 749
Shapley, A., et al. 2001, ApJ, 562, 95
Shapley, A., et al. 2005, ApJ, 626, 698
Shi, Y., et al. 2005, ApJ, 629, 88
Shi, Y., et al. 2007, ApJ, 669, 841
Smail, I., et al. 1999, MNRAS, 308, 1061
Steidel, C., et al. 2004, ApJ, 604, 534
Szokoly, G. P., et al. 2004, ApJS, 155, 271
Tacconi, L., et al. 2002, ApJ, 580, 73
Teplitz, H., et al. 2007, ApJ, 659, 941
Valiante, E., et al. 2007, ApJ, 660, 1060
van Dokkum, P., et al. 2004, ApJ, 611, 703
Veilleux, S., et al. 1995, ApJS, 98, 171
Veilleux, S., et al. 1999, ApJ, 522, 113
Webb, T. M. A., et al. 2003, ApJ, 597, 680
Webb, T. M. A., et al. 2006, ApJ, 636, L17
Weedman, D. W., Le Floc'h, E., Higdon, S. J. U., Higdon, J. L., & Houck, J. R. 2006a, ApJ, 638, 613
Weedman, D., et al. 2006b, ApJ, 653, 101
Weedman, D. W., et al. 2006c, ApJ, 651, 101
White, S. D. M., & Frenk, C. S. 1991, ApJ, 379, 52
Windhorst, R., et al. 2002, ApJS, 143, 113
Wolf, C., et al. 2005, ApJ, 630, 771
Wu, H., et al. 2005, ApJ, 632, 79
Yan, L., et al. 2005, ApJ, 628, 604
Younger, J., et al. 2009, MNRAS, 394, 1685